Immersogeometric fluid–structure interaction modeling and simulation of transcatheter aortic valve replacement

Michael C. H. Wu[a,b], **Heather M. Muchowski**[a,c], **Emily L. Johnson**[a], **Manoj R. Rajanna**[a], **Ming-Chen Hsu**[a,*]

[a]Department of Mechanical Engineering, Iowa State University, 2043 Black Engineering, Ames, Iowa 50011, USA

[b]School of Engineering, Brown University, 184 Hope Street, Providence, Rhode Island 02912, USA

[c]Department of Mathematics, Iowa State University, 396 Carver Hall, Ames, Iowa 50011, USA

Abstract

The transcatheter aortic valve replacement (TAVR) has emerged as a minimally invasive alternative to surgical treatments of valvular heart disease. TAVR offers many advantages, however, the safe anchoring of the transcatheter heart valve (THV) in the patients anatomy is key to a successful procedure. In this paper, we develop and apply a novel immersogeometric fluid–structure interaction (FSI) framework for the modeling and simulation of the TAVR procedure to study the anchoring ability of the THV. To account for physiological realism, methods are proposed to model and couple the main components of the system, including the arterial wall, blood flow, valve leaflets, skirt, and frame. The THV is first crimped and deployed into an idealized ascending aorta. During the FSI simulation, the radial outward force and friction force between the aortic wall and the THV frame are examined over the entire cardiac cycle. The ratio between these two forces is computed and compared with the experimentally estimated coefficient of friction to study the likelihood of valve migration.

1. Introduction

Demand for valve replacement surgery has grown in recent years with the increased prevalence of valvular heart disease [1, 2]. The most popular type of replacement valves continues to be bioprosthetic heart valves (BHV), which are fabricated from xenograft

*Corresponding author: jmchsu@iastate.edu (Ming-Chen Hsu).

biomaterials. These are used for both established surgical and more novel percutaneous valve designs [3–6]. However, the durability of BHVs remains limited, mostly due to structural deterioration caused by fatigue and tissue mineralization [7–10]. Due to the limited lifetime of BHVs, patients may require multiple replacement surgeries, which can cause an increased rate of complications, particularly in elderly patients with comorbidities.

Percutaneous interventions, such as the transcatheter aortic valve replacement (TAVR), have emerged as minimally invasive alternatives to surgical treatment of various valvular diseases [11]. A percutaneous prosthetic valve is deployed through a catheter and anchored to the aortic annulus over the calcified leaflets, displacing the diseased valve and assuming its role. In contrast, the surgical BHV requires an open-heart surgery to suture the device to the annulus. Due to lower operative risk, decreased postoperative pain, and faster rehabilitation compared to surgical treatments, percutaneous valve replacement is becoming a more attractive therapeutic modality in the management of various valvular defects, especially for patients who are considered to be of high or prohibitive surgical risk.

The safe anchoring of the prosthesis in the patient's anatomy is key to a successful TAVR procedure. The fully expanded frame of most transcatheter heart valves (THV) is designed to be oversized with respect to the diameter of the aortic annulus. However, excessive oversizing may increase the risk for coronary obstruction, conduction disturbances, atrioventricular block, periaortic hematoma, and annular rupture [12–17], while insufficient oversizing may lead to poor device fixation, valve migration, paravalvular regurgitation, and prosthetic embolism [18–26]. Thus, selection of an appropriately sized THV is the one of the most significant tasks in TAVR procedures. This can be challenging as the final size of the THV after implantation depends on the stiffness and elasticity of the surrounding anatomy and the mechanical properties of the device. These interactions between the artery and frame should be considered to assess the effectiveness of an implanted frame [27]. The U.S. Food and Drug Administration (FDA) recommends measuring the radial outward force of the THV frame against the artery wall after deployment [28]. For the purpose of pre-operative planning, computational simulations of TAVR provide an effective way to predict the interaction between the THV and the surrounding anatomy.

The THV system has been studied using structural mechanics simulations [29–34], computational fluid dynamics [35, 36], and fluid–structure interaction (FSI). Kandail et al. [37] applied FSI simulations to study the impact of deployment location for the Medtronic CoreValve and found that when the device is deployed at the supra-annular position, the wall shear stress on the outer-curvature of the ascending aorta is significantly elevated. Wu et al. [38] performed FSI simulations to study TAVR with two different models of aortic roots, an idealized straight rigid tube and a patient-specific elastic root, and found that the results from each model differ in many aspects, especially for hemodymanics and the strain distribution on the frame after deployment. Ghosh et al. [39] compared the performance of transcatheter and surgical valves using FSI simulations and found that THVs produced a larger opening area and higher flow rate than the surgical valves, while the stress magnitudes on the valves were of the same order.

Several research groups have also used structural simulations to study the radial outward force of the THV frame. This is of particular interest because the THV's anchoring mechanism relies on oversizing. Tzamtzis et al. [40] analyzed the radial force produced by the 26 mm Medtronic CoreValve and Edwards SAPIEN, and found that the radial force may vary considerably within the recommended functional range for the valve implantation. Egron et al. [41] studied radial force profiles of five commercialized THVs to help understand the mechanical behavior of percutaneous valves and find the optimal oversizing strategy. Cabrera et al. [42] computed the radial force produced by the self-expandable frames, and found that frame radial forces exceeding 16 N may induce medial damage and forces of approximately 17.5 N can damage the adventitial layer. They hypothesized that 16 N could be indicative of frame-induced vascular growth and remodeling.

The goal of this paper is to develop a computational FSI framework for TAVR simulations in order to analyze both the radial outward force and the friction force of the multiphysics THV system. These forces can be used to estimate the ratio of the friction force magnitude to radial force magnitude, which is necessary for studying THV anchoring and estimating the possibility of migration. To the best of our knowledge, analysis of the radial outward force and friction force simultaneously using FSI simulations has never been achieved. In this work, we first propose methods to geometrically model a THV using an IGA-based parametric design platform [43, 44]. A THV typically has three main components: the frame, the skirt, and the leaflets. The coupling among the components introduces major challenges in simulating such a system. Building upon the immersogeometric FSI framework [45–53], which is a technology that directly immerses the computer-aided design geometry into an independent discretization of the surrounding fluid space, we introduce the following new modeling features. The THV frame is modeled using an extension of the isogeometric Bernoulli beam formulation proposed by Bauer et al. [54]; the method is extended in order to handle complex geometries. The THV leaflets and skirt are modeled using anisotropic hyperelastic isogeometric Kirchhoff–Love shells [51]. We apply a penalty method [55] to couple adjacent patches between the skirt and leaflets, and propose methods to couple the skirt and frame, as well as the frame and fluids. With the proposed technology, we simulate the coupled dynamics of the aortic root, the THV, and the surrounding blood flow under physiological conditions to study the static friction coefficient between the deforming aortic wall and THV frame.

This paper is organized as follows. In Section 2, we introduce the mathematical model and solution techniques for the THV FSI problem. Methods to model the interactions of the various components of the THV system are proposed. In Section 3, we describe in detail the geometry modeling process for the THV and aorta. In Section 4, we test the new technology proposed for the frame with multiple benchmark problems. We then demonstrate the capability of our framework by applying the proposed methods to the FSI simulation of a THV under physiologically realistic setup and conditions. Finally, the conclusions are presented in Section 5.

2.   Simulation framework

In this section, we present the main constituents of the FSI framework used for modeling the THV system. The FSI problem consists of the blood flow, the arterial wall, and the various components of the THV. The formulation for each component is discussed in detail along with the methods proposed to model the interactions of the several components of the THV system.

2.1.   Fluid–structure interaction problem

The THV and ascending aorta at time t are modeled as elastic structures occupying region $(\Omega_s)_t$, coupled to blood flow through $(\Omega_f)_t$ by kinematic and traction compatibility conditions at the fluid–structure interface $(\Gamma_I)_t$. The blood flow within $(\Omega_f)_t$ is assumed to be incompressible and Newtonian. The subscript t may be omitted in some formulas below, when there is no risk of confusion. This coupled partial differential equation (PDE) system can be expressed in weak form as: Find a fluid velocity $\mathbf{u}_f \in \mathcal{S}_u$, fluid pressure $p \in \mathcal{S}_p$, structure displacement $y \in \mathcal{S}_y$, and a fluid–solid interface Lagrange multiplier $\lambda \in \mathcal{S}_\ell$ such that for all $\mathbf{w}_f \in \mathcal{V}_u$, $q \in \mathcal{V}_q$, $\mathbf{w}_s \in \mathcal{V}_y$, and $\delta\lambda \in \mathcal{V}_\ell$,

$$
\begin{aligned}
& B_f(\{\mathbf{w}_f, q\}, \{\mathbf{u}_f, p\}) - F_f(\{\mathbf{w}_f, q\}) + B_s(\mathbf{w}_s, \mathbf{y}) - F_s(\mathbf{w}_s) \\
& + \int_{\Gamma_1} (\mathbf{w}_f - \mathbf{w}_s) \cdot \lambda \, d\Gamma + \int_{\Gamma_1} \delta\lambda \cdot (\mathbf{u}_f - \mathbf{u}_s) d\Gamma \\
& + \int_{\Gamma_1} (\mathbf{w}_f - \mathbf{w}_s) \cdot \beta(\mathbf{u}_f - \mathbf{u}_s) d\Gamma = 0,
\end{aligned}
\tag{1}
$$

where $\mathcal{S}_{(\cdot)}$ and $\mathcal{V}_{(\cdot)}$ are trial solution and test function spaces, B_f, B_s, F_f, and F_s are variational forms defining the fluid and structure subproblems, $\mathbf{u}_s$ is the material time derivative of $\mathbf{y}$, and β is a penalty parameter. The terms integrated over Γ_I enforce the fluid–structure coupling conditions on the fluid–structure interface. The presence of these terms facilitates the development of certain numerical schemes based on the "augmented Lagrangian" concept, as elaborated in Bazilevs et al. [56]. The forms defining the fluid and structure subproblems are defined in the following sections.

2.2.   Fluid formulation

The blood flow in a deforming artery is governed by the Navier–Stokes equations of incompressible flows posed on a moving domain. The fluid subproblem in (1) is given in the arbitrary Lagrangian–Eulerian (ALE) description [57] as follows:

$$
\begin{aligned}
& B_f(\{\mathbf{w}_f, q\}, \{\mathbf{u}_f, p\}) - F_f(\{\mathbf{w}_f, q\}) \\
& = \int_{(\Omega_f)_t} \mathbf{w}_f \cdot \rho_f \left(\left. \frac{\partial \mathbf{u}_f}{\partial t} \right|_{\hat{\mathbf{x}}} + (\mathbf{u}_f - \hat{\mathbf{u}}) \cdot \nabla \mathbf{u}_f \right) d\Omega + \int_{(\Omega_f)_t} \varepsilon(\mathbf{w}_f) : \sigma \, d\Omega + \int_{(\Omega_f)_t} q \nabla \cdot \mathbf{u}_f d\Omega \\
& - \gamma \int_{(\Gamma_f^h)_t} \mathbf{w}_f \cdot \rho_f \{ (\mathbf{u}_f - \hat{\mathbf{u}}) \cdot n_f \}_- \mathbf{u}_f d\Gamma - \int_{(\Omega_f)_t} \mathbf{w}_f \cdot \rho_f \mathbf{f}_f d\Omega \\
& - \int_{(\Gamma_f^h)_t} \mathbf{w}_f \cdot \mathbf{h}_f \\
& \quad d\Gamma,
\end{aligned}
\tag{2}
$$

where ρ_f is the fluid mass density, $\partial(\,\cdot\,)/\partial t|_{\hat{\mathbf{x}}}$ is the time derivative taken with respect to the fixed coordinates $\hat{\mathbf{x}}$ of the spatial configuration, $\hat{\mathbf{u}}$ is the (arbitrary) velocity with which the fluid sub-problem domain $(\Omega_f)_t$ deforms, ∇ is the gradient taken with respect to the spatial coordinate $\mathbf{x}$ of the current configuration, $\varepsilon(\cdot)$ is the symmetric gradient operator given by $\varepsilon(\mathbf{w}) = \frac{1}{2}\big(\nabla\mathbf{w} + \nabla\mathbf{w}^{\mathrm{T}}\big)$, $\sigma = -p\mathrm{I} + 2\mu_f\varepsilon(\mathbf{u}_f)$ is the fluid Cauchy stress, μ_f is the dynamic viscosity, the $\gamma(\ \ 0)$ term, referred to as backflow stabilization [58], improves the well-posedness of the problem when there is significant inflow through the Neumann boundary Γ_f^h, $\{\,\cdot\,\}_-$ isolates the negative part of its argument, $\mathbf{n}_f$ is the outward-facing normal vector to the fluid domain, $\mathbf{f}_f$ is a prescribed body force, and $\mathbf{h}_f$ is a prescribed flux on Γ_f^h. This flux is defined as a traction on the outflow portions of the boundary (where $(\mathbf{u}_f - \hat{\mathbf{u}})\cdot\mathbf{n}_f > 0$) and some γ-dependent combination of traction and advective flux on the inflow portion of the boundary [59].

2.3. Structural formulations

This section consists of all the formulations to model the artery wall and the THV, which is composed of the leaflets, skirt, and frame. Based on their thickness relative to the dimension of the system, we model the artery wall as an elastic solid and the valve leaflets and skirt as thin shell structures. The frame is fabricated with long, thin wires which we model using elastic beams. This distinction can be formalized by introducing superscripts "so", "sh", and "be" to denote the solid, shell, and beam, respectively, and expressing $\mathcal{S}_y = \mathcal{S}_y^{\mathrm{so}} \times \mathcal{S}_y^{\mathrm{sh}} \times \mathcal{S}_y^{\mathrm{be}}$ and $\mathcal{V}_y = \mathcal{V}_y^{\mathrm{so}} \times \mathcal{V}_y^{\mathrm{sh}} \times \mathcal{V}_y^{\mathrm{be}}$ such that $\mathbf{y} = \{\mathbf{y}^{\mathrm{so}}, \mathbf{y}^{\mathrm{sh}}, \mathbf{y}^{\mathrm{be}}\}$ and $\mathbf{w}_s = \big\{\mathbf{w}_s^{\mathrm{so}}, \mathbf{w}_s^{\mathrm{sh}}, \mathbf{w}_s^{\mathrm{be}}\big\}$. We can then write

$$B_s(\mathbf{w}_s, \mathbf{y}) = B_s^{\mathrm{so}}(\mathbf{w}_s^{\mathrm{so}}, \mathbf{y}^{\mathrm{so}}) + B_s^{\mathrm{sh}}\big(\mathbf{w}_s^{\mathrm{sh}}, \mathbf{y}^{\mathrm{sh}}\big) + B_s^{\mathrm{be}}\big(\mathbf{w}_s^{\mathrm{be}}, \mathbf{y}^{\mathrm{be}}\big), \tag{3}$$

and

$$F_s(\mathbf{w}_s) = F_s^{\mathrm{so}}(\mathbf{w}_s^{\mathrm{so}}) + F_s^{\mathrm{sh}}\big(\mathbf{w}_s^{\mathrm{sh}}\big) + F_s^{\mathrm{be}}\big(\mathbf{w}_s^{\mathrm{be}}\big). \tag{4}$$

The interaction of the various parts of the THV introduces some major challenges, which will be addressed in this section. This section also introduces methods to couple the adjacent patches between leaflets and skirt, as well as leaflets and frame. In addition, methods to model contact among the various components are also discussed.

2.3.1. Artery wall modeling—The artery wall is modeled as a hyperelastic solid, subject to damping forces. We define

$$\begin{aligned} B_s^{\mathrm{so}}(\mathbf{w}_s, \mathbf{y}) - F_s^{\mathrm{so}}(\mathbf{w}_s) = {}&\int_{(\Omega_s^{\mathrm{so}})_0} \mathbf{w}_s \cdot \rho_s^{\mathrm{so}} \frac{\partial^2 \mathbf{y}}{\partial t^2}\bigg|_{\mathring{\mathbf{x}}} \mathrm{d}\Omega + \int_{(\Omega_s^{\mathrm{so}})_0} \nabla_{\mathring{\mathbf{x}}}\mathbf{w}_s : \mathbf{F}(\mathbf{S}+\mathbf{S}_0)\mathrm{d}\Omega \\ &- \int_{(\Omega_s^{\mathrm{so}})_0} \mathbf{w}_s \cdot \rho_s^{\mathrm{so}}\mathbf{f}_s \mathrm{d}\Omega - \int_{(\Gamma_s^{\mathrm{so},h})_t} \mathbf{w}_s \cdot \mathbf{h}_s \mathrm{d}\Gamma, \end{aligned} \tag{5}$$

where $(\Omega_s^{so})_0$ is the portion of Ω_s corresponding to the artery wall in the reference configuration, ρ_s^{so} is the solid mass density, $\partial(\,\cdot\,)/\partial t|_{\mathring{\mathbf{x}}}$ is the time derivative holding the material coordinates $\mathring{\mathbf{x}}$ fixed, $\nabla_{\mathring{\mathbf{x}}}^{\circ}$ is the gradient operator on $(\Omega_s^{so})_0$, $\mathbf{F}$ is the deformation gradient associated with displacement $\mathbf{y}$, $\mathbf{S}$ is the hyperelastic contribution to the second Piola–Kirchhoff stress tensor, $\mathbf{S}_0$ is a prescribed prestress tensor [60, 61], $\mathbf{f}_s$ is a prescribed body force, and $\mathbf{h}_s$ is a prescribed traction on the Neumann boundary $\Gamma_s^{so,\,h}$.

In this work, the elastic contribution to the second Piola–Kirchhoff stress in Eq. (5) is derived from a compressible neo-Hookean model with dilatational penalty [60, 62]:

$$\psi = \frac{\mu_s^{so}}{2}\left(J^{-2/3}I_1 - 3\right) + \frac{\kappa_s^{so}}{2}\left(\frac{1}{2}\left(J^2 - 1\right) - \ln J\right), \tag{6}$$

$$\mathbf{S} = 2\frac{\partial \psi}{\partial \mathbf{C}} = \mu_s^{so}J^{-2/3}\left(\mathbf{I} - \frac{1}{3}I_1\mathbf{C}^{-1}\right) + \frac{\kappa_s^{so}}{2}\left(J^2 - 1\right)\mathbf{C}^{-1}, \tag{7}$$

where μ_s^{so} and κ_s^{so} are the shear and bulk moduli, respectively, $J = \det \mathbf{F}$ is the Jacobian determinant, $\mathbf{C} = \mathbf{F}^{\mathrm{T}}\mathbf{F}$ is the right Cauchy–Green deformation tensor, $I_1 = \mathrm{tr}\,\mathbf{C}$ is the first invariant of $\mathbf{C}$, and $\mathbf{I}$ is the identity tensor. The stress–strain behavior of model (7) was discussed in Bazilevs et al. [60] and shown to be appropriate for arterial wall modeling in FSI simulations.

The additional pressure $\mathbf{S}_0$ in Eq. (5) is required because the initial aorta configuration is subject to blood pressure and viscous traction and is therefore not stress-free. We follow the procedure from Xu et al. [50] to determine $\mathbf{S}_0$. Begin by setting the displacement from the reference configuration to zero in (5) and assume that external forces on the solid subproblem are due to interaction with the fluid. This leaves us with the problem: Find the symmetric tensor $\mathbf{S}_0$ such that for all $\mathbf{w}_s \in \mathcal{V}_y^{so}$,

$$\int_{(\Omega_s^{so})_0} \nabla_{\mathring{\mathbf{x}}}^{\circ}\mathbf{w}_s : \mathbf{S}_0 \, \mathrm{d}\Omega + \int_{(\Gamma_I^{so})_0} \mathbf{w}_s \cdot \widetilde{\mathbf{h}}_f \, \mathrm{d}\Gamma = 0, \tag{8}$$

where $(\Gamma_I^{so})_0 = (\Gamma_I)_0 \cap \overline{(\Omega_s^{so})_0}$, the notation $\overline{A}$ indicates the topological closure of a set A, and $\widetilde{\mathbf{h}}_f$ is a prescribed fluid traction, which may be obtained from a separate rigid-wall blood flow simulation on the reference domain with appropriate boundary conditions.

2.3.2. Thin shell formulations for the leaflets and skirt—The leaflets and skirt are thin tissue structures and are modeled as hyperelastic isogeometric Kirchhoff–Love shells [63]. The Kirchhoff–Love hypothesis of straight and normal cross sections implies that a point $\mathbf{x}$ in the shell continuum can be described by a point $\mathbf{r}$ on the midsurface and a vector $\mathbf{a}_3$ normal to the midsurface: $\mathbf{x}(\xi^1, \xi^2, \xi^3) = \mathbf{r}(\xi^1, \xi^2) + \xi^3\,\mathbf{a}_3(\xi^1, \xi^2)$, where ξ^1, ξ^2 are the contravariant coordinates of the midsurface, $\xi^3 \in [-H/2, H/2]$ is the through-thickness coordinate, and H is the shell thickness.

Covariant base vectors and metric coefficients of the convective curvilinear coordinate system are defined by $\mathbf{g}_i = \mathbf{x}_{,i}$ and $g_{ij} = \mathbf{g}_i \cdot \mathbf{g}_j$, respectively, where $(\cdot)_{,i} = \partial(\cdot)/\partial\xi^i$. For the shell formulation, we adopt the convention that Latin indices take on values {1, 2, 3}, and Greek indices take on values {1, 2} to denote the in-plane components. Contravariant base vectors $\mathbf{g}i$ are defined by $\mathbf{g}^i \cdot \mathbf{g}_j = \delta^i_j$ and contravariant metric coefficients are given by $[g^{ij}] = [g_{ij}]^{-1}$. For the Kirchhoff–Love shell theory, both normal and transverse shear strains are neglected; only the in-plane strain components are considered. The theory assumes a linear strain distribution through the thickness and defines $g_{\alpha\beta} = a_{\alpha\beta} - 2\,\xi^3 b_{\alpha\beta}$, where $a_{\alpha\beta} = \mathbf{a}_\alpha \cdot \mathbf{a}_\beta$, $b_{\alpha\beta} = \mathbf{a}_{\alpha,\beta} \cdot \mathbf{a}_3$, $\mathbf{a}_\alpha = \mathbf{r}_{,\alpha}$, $\mathbf{a}_3 = (\mathbf{a}_1 \times \mathbf{a}_2)/\|\mathbf{a}_1 \times \mathbf{a}_2\|$, and $\|\cdot\|$ is the Euclidean norm. These definitions hold for both deformed and undeformed configurations where variables of the latter are indicated by $(\mathring{\,\cdot\,})$, for example, $\mathring{\mathbf{x}}$, $\mathring{\mathbf{g}}_{,i}$, $\mathring{g}_{ij}$, etc. The Jacobian determinant of the structure's motion is $J = \sqrt{|g_{ij}|/|\mathring{g}_{ij}|}$ and the in-plane Jacobian determinant is $\bar{J} = \sqrt{|g_{\alpha\beta}|/|\mathring{g}_{\alpha\beta}|}$. The weak form of the shell structural formulation is defined as,

$$
B_s^{\mathrm{sh}}(\mathbf{w}_s, \mathbf{y}) - F_s^{\mathrm{sh}}(\mathbf{w}_s) = \int_{(\mathscr{S}^{\mathrm{sh}})_0} \mathbf{w}_s \cdot \rho_s^{\mathrm{sh}} H \left. \frac{\partial^2 \mathbf{y}}{\partial t^2} \right|_{\mathring{\mathbf{x}}} \mathrm{d}\mathscr{S} + \int_{(\mathscr{S}^{\mathrm{sh}})_0} \int_{-\frac{H}{2}}^{\frac{H}{2}} \delta\mathbf{E}:\mathbf{S}\, \mathrm{d}\xi^3 \mathrm{d}\mathscr{S}
$$
$$
- \int_{(\mathscr{S}^{\mathrm{sh}})_0} \mathbf{w}_s \cdot \rho_s^{\mathrm{sh}} H \mathbf{f}_s\, \mathrm{d}\mathscr{S} - \int_{(\mathscr{S}^{\mathrm{sh}})_t} \mathbf{w}_s \cdot \mathbf{h}_s^{\mathrm{net}} \mathrm{d}\mathscr{S},
\tag{9}
$$

where $(\mathscr{S}^{\mathrm{sh}})_0$ and $(\mathscr{S}^{\mathrm{sh}})_t$ are the shell midsurfaces in the reference and deformed configurations, $\mathbf{y}$ is the midsurface displacement, ρ_s^{sh} is the shell density, $\mathbf{S}$ is the second Piola–Kirchhoff stress tensor obtained from a hyperelastic strain energy density functional ψ: $\mathbf{S} = \partial_{\mathbf{E}}\psi$, $\mathbf{E} = \frac{1}{2}(\mathbf{C}-\mathbf{I})$ is the Green–Lagrange strain tensor, $\mathbf{C}$ is the right Cauchy–Green deformation tensor, $\mathbf{I}$ is the identity tensor, $\delta\mathbf{E}$ is the variation of $\mathbf{E}$ corresponding to displacement variation $\mathbf{w}_s$, $\mathbf{f}_s$ is a prescribed body force, and $\mathbf{h}_s^{\mathrm{net}}$ is the total traction from the two sides of the shell. In this work, we assume the material to be incompressible; the elastic strain energy functional ψ_{el} is augmented by a constraint term enforcing $J = \sqrt{\det \mathbf{C}} = 1$, via a Lagrange multiplier p: $\psi = \psi_{el} - p(J - 1)$.

Using kinematic assumptions and mathematical manipulations given by Kiendl et al. [63], the in-plane Green–Lagrange strain $E_{\alpha\beta}$ can be split into membrane and curvature contributions,

$$
E_{\alpha\beta} = \varepsilon_{\alpha\beta} + \xi^3 \kappa_{\alpha\beta},
\tag{10}
$$

where $\varepsilon_{\alpha\beta} = \frac{1}{2}(a_{\alpha\beta} - \mathring{a}_{\alpha\beta})$ and $\kappa_{\alpha\beta} = \mathring{b}_{\alpha\beta} + b_{\alpha\beta}$ are the membrane strain and change of curvature tensors, respectively, at the shell mid-surface. For incompressible materials, one can express E_{33} in terms of $E_{\alpha\beta}$ [63, Eq. (38)], formally eliminate the Lagrange multiplier p using the plane-stress condition, $S^{33} = 0$ [63, Eq. (46)], and derive an in-plane material tangent tensor $\widehat{\mathbb{C}}$ such that $\mathrm{d}S^{\alpha\beta} = \widehat{\mathbb{C}}^{\alpha\beta\gamma\delta}\mathrm{d}E_{\gamma\delta}$, where $\mathrm{d}\mathbf{S}$ and $\mathrm{d}\mathbf{E}$ are total differentials of $\mathbf{S}$ and $\mathbf{E}$:

$$S^{\alpha\beta} = 2\frac{\partial \psi_{el}}{\partial C_{\alpha\beta}} - 2\frac{\partial \psi_{el}}{\partial C_{33}}J_o^{-2}g^{\alpha\beta}, \tag{11}$$

$$\begin{aligned}
\widehat{\mathbb{C}}^{\alpha\beta\gamma\delta} &= 4\frac{\partial^2 \psi_{el}}{\partial C_{\alpha\beta}\partial C_{\gamma\delta}} + 4\frac{\partial^2 \psi_{el}}{\partial C_{33}^2}J_o^{-4}g^{\alpha\beta}g^{\gamma\delta} - 4\frac{\partial^2 \psi_{el}}{\partial C_{33}\partial C_{\alpha\beta}}J_o^{-2}g^{\gamma\delta} - 4\frac{\partial^2 \psi_{el}}{\partial C_{33}\partial C_{\gamma\delta}}J_o^{-2}g^{\alpha\beta} \\
&\quad + 2\frac{\partial \psi_{el}}{\partial C_{33}}J_o^{-2}(2g^{\alpha\beta}g^{\gamma\delta} + g^{\alpha\gamma}g^{\beta\delta} + g^{\alpha\delta}g^{\beta\gamma})
\end{aligned} \tag{12}$$

.

With Eqs. (11) and (12), arbitrary 3D constitutive models providing $\frac{\partial \psi_{el}}{\partial C_{ij}}$ and $\frac{\partial^2 \psi_{el}}{\partial C_{ij}\partial C_{kl}}$ can be directly used for shell analysis.

In this work, we model the constitutive behavior of THV leaflets and skirt using a transversely isotropic (Lee–Sacks) model [51, 64]. This model's strain energy functional uses a neo-Hookean term to model the extracellular matrix and a convex combination of fully-isotropic and transversely-isotropic exponential-type terms to model the network of collagen fibers. The model is given by

$$\psi_{el}(I_1, I_4) = \frac{c_0}{2}(I_1 - 3) + \frac{c_1}{2}\left(we^{c2(I_1-3)^2} + (1-w)e^{c3(I_4-1)^2} - 1\right), \tag{13}$$

where c_0, c_1, c_2, c_3 are material parameters, $w \in [0, 1]$ determines the strain energy contribution due to anisotropy[1], $I_1 = \text{tr } \mathbf{C}$, and $I_4 = \mathbf{m} \cdot \mathbf{C} \mathbf{m}$, where $\mathbf{m}$ is a unit vector defining the collagen fiber direction in the reference configuration. Based on the structure of the bovine or porcine pericardium used in THVs, we assume that collagen fibers lie primarily in the plane of the tissue. (i.e., $m^3 = 0$ in the curvilinear system).

2.3.3. Bernoulli beam formulations for the frame

—The frame is fabricated with long, thin wires and is modeled using an extension of the isogeometric Bernoulli beam. Bauer et al. [54] proposed a spatially curved and geometrically nonlinear isogeometric beam formulation derived based on Bernoulli kinematics. The geometric description was adapted from the spatial rod of Greco and Cuomo [65]. The formulation proposed by Bauer et al. [54] has four degrees of freedom, three for displacements and one for the rotation about the beam centerline, and is effective for modeling simple geometries. However, for more complex structures such as the THV frame, an extension proposed in this work is needed to handle the geometric complexity.

In this section, Latin indices take on values {1, 2, 3} while Greek indices take on values {2, 3}. The continuum of the beam is described by a centerline and a moving local coordinate system, which is used to describe the orientation of the cross section. The position vector $\mathbf{x}$ for the continuum of the beam is defined as

---

[1]Note that the exponential anisotropic term asymptotically dominates the isotropic term with increasing strain. For any $z > 0$, no matter how small, if $w = 1 - \epsilon$, there exists a strain level beyond which the anisotropic term dominates.

$$\mathbf{x}\left(\xi^1, \xi^2, \xi^3\right) = \mathbf{r}\left(\xi^1\right) + \xi^2 \mathbf{a}_2\left(\xi^1\right) + \xi^3 \mathbf{a}_3\left(\xi^1\right), \tag{14}$$

where ξ^1 is the contravariant coordinate of the centerline, ξ^2 and ξ^3 are coordinates of the cross section, $\mathbf{r}$ is the position vector of the centerline, and $\mathbf{a}_2$ and $\mathbf{a}_3$ are base vectors tangent to the cross section; the $\mathbf{a}_\alpha$ vectors are defined such that they are unit vectors and orthogonal to $\mathbf{a}_1$, which is the tangent vector of the centerline calculated as $\mathbf{a}_1 = \mathbf{r}_{,1}$. The $\mathbf{a}_i$ vectors define the moving local coordinate system. Note that $\mathbf{a}_1$ is not a unit vector. These definitions hold for both deformed and undeformed configurations, where variables of the latter are indicated by $(\overset{\circ}{\cdot})$.

The Bernoulli theory assumes that beam cross sections remain orthogonal to the centerline and the cross-sectional dimensions remain unchanged throughout deformation. The cross section itself can develop torsional shear deformation. The two components $\overset{\circ}{\mathbf{a}}_\alpha$ of the moving local basis at every location along the beam centerline in the undeformed configuration are obtained as

$$(\overset{\circ}{\mathbf{a}}_\alpha)_i = \mathbf{R}\left((\overset{\circ}{\hat{\mathbf{a}}}_1)_i, \overset{\circ}{\theta}_i\right)\mathbf{\Lambda}\left(\mathbf{A}_1, (\overset{\circ}{\hat{\mathbf{a}}}_1)_i\right)\mathbf{A}_\alpha, \text{ for } i = 1, \dots, n, \tag{15}$$

where the three unit vectors $\mathbf{A}_1$ and $\mathbf{A}_\alpha$ define a global reference coordinate system, $\mathbf{\Lambda}$ is a mapping operator that maps one vector to the other, $\mathbf{R}$ is the rotation operator, $\widehat{(\cdot)}$ denotes the normalized vector, and i and n denote the ith location and number of points along the centerline, respectively. The mapping and rotation operators used for the beam formulation are designed based on the Euler–Rodrigues formula specialized to the current problem (see Bauer et al. [54] for details), given as

$$\mathbf{\Lambda}\left(\hat{\mathbf{t}}_0, \hat{\mathbf{t}}\right) = \left(\hat{\mathbf{t}}_0 \cdot \hat{\mathbf{t}}\right)\mathbf{I} + \left(\hat{\mathbf{t}}_0 \times \hat{\mathbf{t}}\right) \times \mathbf{I} + \frac{1}{1 + \hat{\mathbf{t}}_0 \cdot \hat{\mathbf{t}}}\left(\hat{\mathbf{t}}_0 \times \hat{\mathbf{t}}\right) \otimes \left(\hat{\mathbf{t}}_0 \times \hat{\mathbf{t}}\right) \tag{16}$$

and

$$\mathbf{R}\left(\hat{\mathbf{t}}, \phi\right) = \cos(\phi)\mathbf{I} + \sin(\phi)\hat{\mathbf{t}} \times \mathbf{I}, \tag{17}$$

where $\hat{\mathbf{t}}_0$ and $\hat{\mathbf{t}}$ are normalized vectors, $\mathbf{\Lambda}\left(\hat{\mathbf{t}}_0, \hat{\mathbf{t}}\right)$ maps a vector through aligning $\hat{\mathbf{t}}_0$ to $\hat{\mathbf{t}}$, and $\mathbf{R}\left(\hat{\mathbf{t}}, \phi\right)$ rotates a vector that is orthogonal to $\hat{\mathbf{t}}$ by an angle φ about $\hat{\mathbf{t}}$. The definition of the cross product between a vector $\mathbf{v}$ and a matrix $\mathbf{M}$ is $(\mathbf{v} \times \mathbf{M})_{il} = \epsilon_{ijk} v_j \mathbf{M}_{kl}$, where ϵ_{ijk} is the permutation symbol. Equation (15) maps $\mathbf{A}_\alpha$ so that $\mathbf{A}_1$ is aligned to $\overset{\circ}{\mathbf{a}}_1$, the tangent along the centerline, then rotates the new base vectors $\mathbf{a}'_\alpha = \mathbf{\Lambda}\left(\mathbf{A}_1, \overset{\circ}{\hat{\mathbf{a}}}_1\right)\mathbf{A}_\alpha$ by an angle $\overset{\circ}{\theta}$ about $\overset{\circ}{\mathbf{a}}_1$ to the desired orientation where the cross-sectional profile of the beam geometry is defined. The same two steps of mapping and rotation can be adapted to describe the alignment of the moving local coordinate system from the undeformed to the deformed configuration:

$$\mathbf{a}_\alpha = \mathbf{R}(\hat{\mathbf{a}}_1, \theta)\mathbf{\Lambda}(\overset{\circ}{\hat{\mathbf{a}}}_1, \hat{\mathbf{a}}_1)\overset{\circ}{\mathbf{a}}_\alpha, \tag{18}$$

where θ is a rotational degree of freedom.

For simple geometries, the definition of the local coordinate basis described in Eq. (15) is effective. However, for modeling complex structures, like the THV frame, this formulation shows some limitations. Based on observations, the formulation was not effective for locations where the tangents of the centerline change significantly over a small increment. This is due to the fact that the mapping operator defined in Eq. (15) maps a global reference coordinate system to the local coordinate system at given locations along the centerline; this mapping causes $\mathbf{a}'_\alpha$ to have high variance when the locations along the centerline are too far apart, however, when the increments are small, the $\mathbf{a}'_\alpha$ only change a small amount from one location to the next. This increase in the variance of $\mathbf{a}'_\alpha$ causes a large difference in $\mathring{\theta}$ between two neighboring locations, and the large change in $\mathring{\theta}$ causes a twisting effect in the geometry when interpolation is used to evaluate $\mathring{\theta}$.

In this work, we propose a remedy to decrease the variance in the moving $\mathbf{a}'_\alpha$ by mapping from a neighboring point as opposed to the global coordinate system. Let $(\mathbf{a}'_\alpha)_1 = \mathbf{\Lambda}(\mathbf{A}_1, (\hat{\mathbf{a}}_1)_1)\mathbf{A}_\alpha$ and denote $(\mathbf{a}'_\alpha)_i$ as the vectors $\mathbf{a}'_\alpha$ at the ith location. Then, define

$$(\mathbf{a}'_\alpha)_i = \mathbf{\Lambda}((\hat{\mathbf{a}}_1)_{i-1}, (\hat{\mathbf{a}}_1)_i)(\mathbf{a}'_\alpha)_{i-1}, \text{ for } i = 2, \ldots, n, \tag{19}$$

where n is the number of points along the centerline. In this work, each $(\mathbf{a}'_\alpha)_i$ is evaluated on the quadrature points. This can then be combined with the rotation operator to obtain the final formulation at every location along the centerline,

$$(\mathring{\mathbf{a}}_\alpha)_i = \mathbf{R}((\hat{\mathring{\mathbf{a}}}_1)_i, \mathring{\theta}_i)(\mathbf{a}'_\alpha)_i. \tag{20}$$

By using this method, we are able to avoid twisting at locations where the tangents of the centerline change significantly and achieve the desired complex geometry of the THV frame.

Next, we define the covariant base vectors of the continuum as

$$\mathbf{g}_1\left(\xi^1, \xi^2, \xi^3\right) = \mathbf{x}_{,1}\left(\xi^1, \xi^2, \xi^3\right) = \mathbf{a}_1\left(\xi^1\right) + \xi^2 \mathbf{a}_{2,1}\left(\xi^1\right) + \xi^3 \mathbf{a}_{3,1}\left(\xi^1\right), \tag{21}$$

$$\mathbf{g}_\alpha\left(\xi^1\right) = \mathbf{x}_{,\alpha}\left(\xi^1, \xi^2, \xi^3\right) = \mathbf{a}_\alpha\left(\xi^1\right). \tag{22}$$

Again, these definitions hold for both deformed and undeformed configurations, where variables of the latter are indicated by $(\mathring{\cdot})$. The first covariant component E_{11} of the Green–Lagrange strain $\mathbf{E}$ can be obtained as

$$E_{11} = \frac{1}{2}\left(\mathbf{g}_1 \cdot \mathbf{g}_1 - \mathring{\mathbf{g}}_1 \cdot \mathring{\mathbf{g}}_1\right) = \varepsilon + \xi^2 \kappa_{21} + \xi^3 \kappa_{31}, \tag{23}$$

where $\varepsilon = \frac{1}{2}(\mathbf{a}_1 \cdot \mathbf{a}_1 - \mathring{\mathbf{a}}_1 \cdot \mathring{\mathbf{a}}_1)$ and $\kappa_{\alpha 1} = \mathbf{a}_{\alpha,1} \cdot \mathbf{a}_1 - \mathring{\mathbf{a}}_{\alpha,1} \cdot \mathring{\mathbf{a}}_1$ are the axial strain and changes in curvature due to bending, respectively. With the Bernoulli assumption (see Bauer et al. [54] for details), the torsional shear strain is computed as

$$E_{12} = \frac{1}{2}(\mathbf{g}_1 \cdot \mathbf{g}_2 - \mathring{\mathbf{g}}_1 \cdot \mathring{\mathbf{g}}_2) = \frac{1}{2}\xi^2 \kappa_{32}, \tag{24}$$

$$E_{13} = \frac{1}{2}(\mathbf{g}_1 \cdot \mathbf{g}_3 - \mathring{\mathbf{g}}_1 \cdot \mathring{\mathbf{g}}_3) = \frac{1}{2}\xi^2 \kappa_{23}, \tag{25}$$

where $\kappa_{32} = (\mathbf{a}_{3,1} \cdot \mathbf{a}_2 - \mathring{\mathbf{a}}_{3,1} \cdot \mathring{\mathbf{a}}_2)$ and $\kappa_{23} = (\mathbf{a}_{2,1} \cdot \mathbf{a}_3 - \mathring{\mathbf{a}}_{2,1} \cdot \mathring{\mathbf{a}}_3)$ are the changes in curvature due to torsion and $\kappa_{23} = -\kappa_{32}$.[2] Furthermore, since operators $\mathbf{\Lambda}$ and $\mathbf{R}$ commute [65], one can define $\mathbf{Q} = \mathbf{R}(\hat{\mathbf{a}}_1, \theta)\mathbf{\Lambda}(\hat{\mathring{\mathbf{a}}}_1, \hat{\mathbf{a}}_1)$ and derive

$$\begin{aligned}\mathbf{g}_\alpha \cdot \mathbf{g}_\beta &= \mathbf{a}_\alpha \cdot \mathbf{a}_\beta = (\mathbf{Q}\mathring{\mathbf{a}}_\alpha) \cdot (\mathbf{Q}\mathring{\mathbf{a}}_\beta) = \left((\mathbf{Q}^{\mathrm{T}}\mathbf{Q})\mathring{\mathbf{a}}_\beta\right) \cdot \mathring{\mathbf{a}}_\alpha = \left((\mathbf{Q}^{-1}\mathbf{Q})\mathring{\mathbf{a}}_\beta\right) \cdot \mathring{\mathbf{a}}_\alpha \\ &= (\mathbf{I}\mathring{\mathbf{a}}_\beta) \cdot \mathring{\mathbf{a}}_\alpha = \mathring{\mathbf{a}}_\alpha \cdot \mathring{\mathbf{a}}_\beta = \mathring{\mathbf{g}}_\alpha \cdot \mathring{\mathbf{g}}_\beta.\end{aligned} \tag{26}$$

Note that $\mathbf{Q}$ is orthogonal and hence $\mathbf{Q}^{\mathrm{T}} = \mathbf{Q}^{-1}$. Equation (26) yields the following:

$$E_{\alpha\beta} = \frac{1}{2}(\mathbf{g}_\alpha \cdot \mathbf{g}_\beta - \mathring{\mathbf{g}}_\alpha \cdot \mathring{\mathbf{g}}_\beta) = 0. \tag{27}$$

The weak form of the beam subproblem in Eq. (3) is defined as

$$\begin{aligned}B_{\mathrm{s}}^{\mathrm{be}}(\mathbf{w}_{\mathrm{s}}, \mathbf{y}) - F_{\mathrm{s}}^{\mathrm{be}}(\mathbf{w}_{\mathrm{s}}) &= \int_{(\mathscr{L}^{\mathrm{be}})_0} \mathbf{w}_{\mathrm{s}} \cdot \rho_{\mathrm{s}}^{\mathrm{be}} A \left.\frac{\partial^2 \mathbf{y}}{\partial t^2}\right|_{\mathring{\mathbf{x}}} \mathrm{d}\mathscr{L} + \int_{(\mathscr{L}^{\mathrm{be}})_0} \int_A \delta\mathbf{E} : \mathbf{S}\, \mathrm{d}A \mathrm{d}\mathscr{L} \\ &\quad - \int_{(\mathscr{L}^{\mathrm{be}})_0} \mathbf{w}_{\mathrm{s}} \cdot \rho_{\mathrm{s}}^{\mathrm{be}} A \mathbf{f}_{\mathrm{s}}\, \mathrm{d}\mathscr{L} - \int_{(\mathscr{L}^{\mathrm{be}})_t} \mathbf{w}_{\mathrm{s}} \cdot \mathbf{h}_{\mathrm{s}}^{\mathrm{net}}\, \mathrm{d}\mathscr{L},\end{aligned} \tag{28}$$

where $\left(\mathscr{L}^{\mathrm{be}}\right)_t$ and $\left(\mathscr{L}^{\mathrm{be}}\right)_0$ are the centerline of the beam in the deformed and undeformed configurations, respectively, $\rho_{\mathrm{s}}^{\mathrm{be}}$ is the beam density, $\mathbf{h}^{\mathrm{net}}$ is the total traction from two sides of the beam, and A is the cross-sectional area of the beam. In this work, the St. Venant–Kirchhoff material model is applied to the beam. Using the Voigt notation in the following descriptions, the contravariant components of the second Piola–Kirchhoff stress are

$$S^{11} = \frac{E^{\mathrm{be}}}{\left\|\mathring{\mathbf{g}}_1\right\|^2 \left\|\mathring{\mathbf{g}}_1\right\|^2} E_{11}, \tag{29}$$

$$S^{1\alpha} = \frac{\mu_{\mathrm{s}}^{\mathrm{be}}}{\left\|\mathring{\mathbf{g}}_1\right\|^2 \left\|\mathring{\mathbf{g}}_\alpha\right\|^2} 2E_{1\alpha} = \frac{\mu_{\mathrm{s}}^{\mathrm{be}}}{\left\|\mathring{\mathbf{g}}_1\right\|^2} 2E_{1\alpha}, \tag{30}$$

where E^{be}, $\mu_{\mathrm{s}}^{\mathrm{be}} = \dfrac{E^{\mathrm{be}}}{2(1 + v^{\mathrm{be}})}$, and v^{be} are the Young's modulus, shear modulus, and Poisson's ratio of the beam, respectively, described in a Cartesian coordinate system. Note that $\mathbf{g}_\alpha = \mathbf{a}_\alpha$

---

[2]Note that the sign conventions, adapted from literature, used for E_{12} and E_{13}` are based on opposite directions of rotation. As a result, when calculating the total torsional moment based on these torsional shear strains, a subtraction of one moment from the other is needed as shown in Greco and Cuomo [65, Eq. (64)].

are unit vectors. Given the above definitions and pre-integrating over the beam cross-sectional area, the internal virtual work in Eq. (28) becomes

$$
\begin{aligned}
\int_{(\mathscr{L}^{\mathrm{be}})_0} \int_A \delta \mathbf{E} : \mathbf{S} \, \mathrm{d}A \mathrm{d}\mathscr{L} &= \int_{(\mathscr{L}^{\mathrm{be}})_0} \int_A \left(S^{11} \delta E_{11} + S^{12} \delta E_{12} + S^{13} \delta E_{13} \right) \mathrm{d}A \mathrm{d}\mathscr{L} \\
&= \int_{(\mathscr{L}^{\mathrm{be}})_0} \left(\frac{E^{\mathrm{be}}}{\|\mathring{\mathbf{g}}_1\|^4} (A\varepsilon\delta\varepsilon + I_3 \kappa_{21}\delta\kappa_{21} + I_2 \kappa_{31}\delta\kappa_{31}) \right. \\
&\quad \left. + \frac{\mu_s^{\mathrm{be}}}{2\|\mathring{\mathbf{g}}_1\|^2} (I_2 \kappa_{32}\delta\kappa_{32} + I_3 \kappa_{23}\delta\kappa_{23}) \right) \mathrm{d}\mathscr{L},
\end{aligned}
\tag{31}
$$

where $I_3 = \int_A \left(\xi^2\right)^2 \mathrm{d}\xi^2 \mathrm{d}\xi^3$ and $I_2 = \int_A \left(\xi^3\right)^2 \mathrm{d}\xi^2 \mathrm{d}\xi^3$ are the second moments of area about $\mathring{\mathbf{g}}_3$ and $\mathring{\mathbf{g}}_2$, respectively. In the above equations, $\|\mathring{\mathbf{g}}_1\|$ can be approximated as $\|\mathring{\mathbf{a}}_1\|$ for simplicity.

2.3.4. Penalty coupling—In practice, the leaflets and skirt are sutured together and then sutured to the frame. To model the connections between these different components in the simulation, we adapt the penalty coupling approach proposed by Herrema et al. [55]. To enforce the shell–shell coupling of the skirt and leaflets, consider a patch interface $\mathscr{L}_{\mathrm{I}}^{\mathrm{ss}}$ between two shell surface patches $\mathscr{S}^{\mathrm{sh,A}}$ and $\mathscr{S}^{\mathrm{sh,B}}$. Note that the two patches may not have conforming discretizations. In order to impose the displacement continuity at the coupled patch interface, a displacement penalty term is added to $B_{\mathrm{s}}^{\mathrm{sh}}(\mathbf{w}_{\mathrm{s}}, \mathbf{y})$ and is given as

$$
+ \int_{\mathscr{L}_{\mathrm{I}}^{\mathrm{ss}}} \alpha_{\mathrm{d}}^{\mathrm{ss}} \left(\mathbf{w}_{\mathrm{s}}^{\mathrm{sh,A}} - \mathbf{w}_{\mathrm{s}}^{\mathrm{sh,B}} \right) \cdot \left(\mathbf{y}^{\mathrm{sh,A}} - \mathbf{y}^{\mathrm{sh,B}} \right) \mathrm{d}\mathscr{L},
\tag{32}
$$

where $\mathbf{y}^{\mathrm{sh,A}}$ and $\mathbf{y}^{\mathrm{sh,B}}$ are the displacements on surface patches $\mathscr{S}^{\mathrm{sh,A}}$ and $\mathscr{S}^{\mathrm{sh,B}}$, respectively, along the penalty curve $\mathscr{L}_{\mathrm{I}}^{\mathrm{ss}}$, $\mathbf{w}_{\mathrm{s}}^{\mathrm{sh,A}}$ and $\mathbf{w}_{\mathrm{s}}^{\mathrm{sh,B}}$ are their respective weighting functions, and $\alpha_{\mathrm{d}}^{\mathrm{ss}}$ is a variable penalty parameter of large magnitude. For shell–beam coupling of the skirt and the frame, the same displacement penalty approach is used. Thus, the displacement penalty term of the form,

$$
+ \int_{\mathscr{L}_{\mathrm{I}}^{\mathrm{sb}}} \alpha_{\mathrm{d}}^{\mathrm{sb}} \left(\mathbf{w}_{\mathrm{s}}^{\mathrm{sh}} - \mathbf{w}_{\mathrm{s}}^{\mathrm{be}} \right) \cdot \left(\mathbf{y}^{\mathrm{sh}} - \mathbf{y}^{\mathrm{be}} \right) \mathrm{d}\mathscr{L},
\tag{33}
$$

where $\alpha_{\mathrm{d}}^{\mathrm{sb}}$ is an adjustable penalty parameter and $\mathscr{L}_{\mathrm{I}}^{\mathrm{sb}}$ is a penalty curve along the shell–beam interface, is added to $B_{\mathrm{s}}(\mathbf{w}_{\mathrm{s}}, \mathbf{y})$. For the shell–beam coupling, in practice, we choose the penalty curve $\mathscr{L}_{\mathrm{I}}^{\mathrm{sb}}$ to be $\mathscr{L}^{\mathrm{be}}$.

For imposing the rotational continuity between the two shell surfaces, the penalty approach is also used to maintain the angle formed by coupled patch interfaces. A rotational penalty term [55] is added to $B_{\mathrm{s}}^{\mathrm{sh}}(\mathbf{w}_{\mathrm{s}}, \mathbf{y})$ and is given as

$$+ \int_{\mathcal{L}_I^{ss}} \alpha_r^{ss}\Big(\big(\delta\cos\phi - \delta\cos\mathring{\phi}\big)\big(\cos\phi - \cos\mathring{\phi}\big) + \big(\delta\sin\phi - \delta\sin\mathring{\phi}\big)\big(\sin\phi - \sin\mathring{\phi}\big)\Big)\,d\mathscr{L}, \quad (34)$$

where $\mathring{\phi}$ and ϕ are the angles between the surfaces before and after deformation, respectively, and δ denotes the variation. The net-like structure of the THV frame geometry restrains twisting in any local unit of the wire. Thus, we assume the effect of the beam rotation on the shell to be negligible and do not impose a rotational penalty for the shell–beam coupling.

The penalty parameters for shell–shell coupling are given as

$$\alpha_d^{ss} = \alpha^{ss}\frac{E^{sh}H}{h^{sh,I}\big(1 - (v^{sh})^2\big)}, \quad (35)$$

$$\alpha_r^{ss} = \alpha^{ss}\frac{E^{sh}H^3}{12\,h^{sh,I}\big(1 - (v^{sh})^2\big)}, \quad (36)$$

where a^{ss} is a dimensionless penalty coefficient, E^{sh} is some effective material stiffness with units of stress (e.g. the Young's modulus in a linear isotropic material), $h^{sh,I} = \big(h^{sh,A} + h^{sh,B}\big)/2$, $h^{sh,A}$ and $h^{sh,B}$ are the lengths of the local elements in the direction most parallel to the penalty curve, and v^{sh} is the Poisson's ratio. A value of $a^{ss} = 10^3$, as proposed by Herrema et al. [55], is appropriate for the shell–shell coupling in this work. For shell–beam coupling, the following penalty parameter is employed:

$$\alpha_d^{sb} = \alpha^{sb}\min\left\{\frac{E^{sh}H}{h^{sh}\big(1 - (v^{sh})^2\big)}, \frac{E^{be}\sqrt{A}}{h^{be}\big(1 - (v^{be})^2\big)}\right\}, \quad (37)$$

where a^{sb} is a dimensionless penalty coefficient, h^{sh} is defined to be an effective shell element length3, and h^{be} is defined to be the local beam element length. The selection of α_d^{sb} from the minimum parameter value between coupled materials produces a sufficiently high penalty value that is not excessive for the lower stiffness material; the penalty parameter is high enough to ensure constraint satisfaction without creating excessive ill-conditioning. In this work, $a^{sb} = 10^4$ for shell–beam coupling. To apply this coupling method to the hyperelastic material model of the leaflets and skirt, E^{sh} is calculated based on the shear modulus of the neo-Hookean term (c_0) in Eq. (13) and v^{sh} is set to 0.5.

2.3.5. Contact formulation—The THV presents multiple contact problems, including leaflet to leaflet, leaflet to frame, and frame to artery wall contact. In this work, a nonlocal contact formulation developed by Kamensky et al. [66] is used to penalize interpenetration

---

3The shell elements are arbitrarily cut by the penalty curve, so the shell element length along the penalty curve may change significantly between neighboring elements. To avoid producing an oscillatory penalty field and unstable simulations, we choose the effective element length to be the average of the shell element lengths in the direction of the penalty curve.

of various structural components at their quadrature points. Consider all structural parts to be a single body with reference configuration Ω_0. For contact between two points, $\mathbf{x}^A$ and $\mathbf{x}^B$, the following contact term is added to $B_s(\mathbf{w}_s, \mathbf{y})$:

$$+ \int_{\Omega_0 \backslash B_R(\mathring{\mathbf{x}}^A)} \int_{\Omega_0} \delta \mathbf{r}^{AB} \cdot \phi_c'(r^{AB}) \frac{\mathbf{r}^{AB}}{r^{AB}} d\mathring{\mathbf{x}}^A d\mathring{\mathbf{x}}^B, \tag{38}$$

where $\mathring{\mathbf{x}}^A$ and $\mathring{\mathbf{x}}^B$ are in Ω_0, $B_R(\mathring{\mathbf{x}}^A)$ is the Euclidean ball of radius R around $\mathring{\mathbf{x}}^A$, $\mathbf{r}^{A,B} = \mathbf{x}^B - \mathbf{x}^A$, $r^{AB} = \|\mathbf{r}^{AB}\|$ and $\phi_c'(r^{AB})$ is a contact kernel. Kamensky et al. [66] developed a nonlocal formulation for arbitrary ϕ_c' and proposed a singular kernel that requires the use of an adaptive time stepping scheme and a specialized nonlinear solver. For simplicity, in this work, we use a linear penalty force to avoid the complicated additions required for a singular kernel, and define the contact kernel as

$$\phi_c'(r^{AB}) = -\max(k_c(r_{max} - r^{AB}), 0), \tag{39}$$

where k_c is a penalty parameter that needs to be sufficiently large and r_{max} is a cutoff distance within which the contact force is active.

2.3.6. Static friction formulation—When the THV is deployed into the aortic root, it expands and anchors itself on the artery wall and diseased leaflets, and stays in place due to the role of friction. The friction force is dependent on the radial outward force of the THV and the roughness and geometry of the aortic wall. In order to model this effect, a simple static friction model is proposed to estimate the friction force, assuming the THV does not slide after it is fully deployed. The friction force is only active at the locations where contact between the frame and the artery wall occurs after deployment. In this model, the tangential component of the distance between the frame and the artery wall is penalized relative to a reference distance, where the reference distance is determined after the frame is fully deployed. Thus, for the static friction between the solid (artery wall) and beam (frame), the following penalty term is added to $B_s(\mathbf{w}_s, \mathbf{y})$ in locations where contact occurs:

$$+ \int_{\Omega_0^{be}} \int_{\Omega_0^{so}} \delta(\mathbf{r})_\tau \cdot \alpha_f |\phi_c'(\|\mathbf{r}\|)| (\|(\mathbf{r})_\tau\| - \|(\mathbf{r}_d)_\tau\|) \frac{(\mathbf{r})}{\|(\mathbf{r})_\tau\|} d\mathring{\mathbf{x}}^{so} d\mathring{\mathbf{x}}^{be}, \text{ for } \|\mathbf{r}\| < r_{max}, \tag{40}$$

where Ω_0^{be} and Ω_0^{so} are the reference configurations of the beam and solid, respectively, $\mathring{\mathbf{x}}^{be} \in \Omega_0^{be}$, $\mathring{\mathbf{x}}^{so} \in \Omega_0^{so}$ subscript "d" indicates the deployed configuration, subscript "τ" indicates the tangential component, $\mathbf{r} = \mathbf{x}^{be} - \mathbf{x}^{so}$, $\mathbf{r}_d = \mathbf{x}_d^{be} - \mathbf{x}_d^{so}$,

$$(\mathbf{r})_\tau = \mathbf{r} - (\mathbf{r} \cdot \mathbf{n})\mathbf{n}, \tag{41}$$

$$(\mathbf{r}_d)_\tau = \mathbf{r}_d - (\mathbf{r}_d \cdot \mathbf{n}_d)\mathbf{n}_d, \tag{42}$$

$\mathbf{n}$ and $\mathbf{n}_d$ are the outward normal vectors on the artery wall in the current and deployed configurations, respectively, α_f is a penalty parameter, and the contact kernel $\phi_c'(\|\mathbf{r}\|)$ is

introduced so that the friction force is proportional to the contact force. In this work, $a_\text{f} = 10^3$ is found to be effective; the value is large enough to avoid sliding between the frame and the artery wall and is small enough to avoid producing ill-conditioned stiffness matrices in the FSI system.

2.4. Immersogeometric discretization of the FSI model

A technology that has shown great promise for valvular FSI simulation is immersogeometric analysis [45–53]. Kamensky et al. [45] and Hsu et al. [46] developed a numerical method that, in the tradition of immersed boundary methods [67–70], allows the structure discretization to move independently of the background fluid mesh. The technique directly captures design geometries in the unfitted analysis mesh, and makes beneficial use of isogeometric analysis (IGA) [71, 72] to discretize both the structural and fluid mechanics subproblems involved in the FSI analysis. Immersogeometric analysis enables us to discretize the subproblems independently, then couple the interactions through constraint equations. In this section, we discuss the immersogeometric discretization of the FSI problem.

2.4.1. Fluid and structure subproblems—The ALE Navier–Stokes subproblem is discretized using a combination of nonuniform rational B-spline (NURBS)-based IGA and the variational multiscale (VMS) approach [73–77], with some modifications to the stabilization parameters to improve mass conservation, as detailed in Kamensky et al. [45, Section 4.4]. The ALE–VMS formulation may be interpreted both as a stabilized formulation and a large-eddy simulation turbulence model; the methodology applies equally well to laminar and turbulent flows and is thus attractive for the current application where the nature of the flow solution is not known a priori. The VMS formulation maintains stability over broad classes of velocity and pressure discrete spaces and we are not restricted to special inf–sup-stable combinations. For computations in this paper, we use an "equal order" discretization scheme—the same scalar discrete space is used to represent the pressure and each Cartesian component of the fluid velocity. On the fluid mechanics domain interior, the mesh velocity $\hat{\mathbf{u}}$ is obtained by solving a fictitious linear elastostatic problem subject to the displacement boundary conditions coming from the motion of the fluid–solid interface from each time step to the next [78–82]. The solid, shell, and beam structures are discretized using IGA and Galerkin method. We use at least C^1-continuous NURBS patches to represent the geometries. NURBS are also used as basis functions for discretization; they can easily provide the required C^1-continuity between elements for the Kirchhoff–Love shell and Bernoulli beam formulations.

2.4.2. Discretization of the fluid–structure kinematic constraint—The artery wall and blood flow domains are chosen to have conforming discretizations at the fluid–solid interface. This automatically satisfies the kinematic and traction compatibility conditions due to the fact that $\mathbf{u}_\text{f} = \mathbf{u}_\text{s}$ and $\mathbf{w}_\text{f} = \mathbf{w}_\text{s}$ at the interface causing the Lagrange multiplier and penalty terms in Eq. (1) to be zeros. This is not the case at the fluid–shell interface; the fluid–shell coupling utilizes the Lagrange multiplier and penalty methods to enforce the kinematic constraints. To take advantage of the weak imposition of no-slip conditions at the fluid–shell interface [56, 83], the tangential component of the Lagrange

multiplier $\boldsymbol{\lambda}$ is formally eliminated leaving only penalty method to weakly enforce the no-slip condition. However, due to the presence of large pressure gradients across the leaflets, the normal component of the Lagrange multiplier $\lambda = \boldsymbol{\lambda} \cdot \mathbf{n}_s^{sh}$, where $\mathbf{n}_s^{sh}$ is the normal vector of the shell midsurface, is retained at the fluid–shell interface in order to strengthen the enforcement of the no-penetration condition. For fluid–beam coupling, we only use penalty to weakly enforce the kinematic constraints due to the fact that the interaction force between the beam and the blood flow is not high.

The discrete variational equation for this FSI system is summarized as follows: Find $\mathbf{u}_f^h \in \mathcal{S}_u^h$, $p^h \in \mathcal{S}_p^h$, $\mathbf{y}^h \in \mathcal{S}_y^h$, and $\lambda \in \mathcal{S}_\ell^h$ such that for all $\mathbf{w}_f^h \in \mathcal{V}_u^h$, $q^h \in \mathcal{V}_q^h$, $\mathbf{w}_s^h \in \mathcal{V}_y^h$, and $\delta\lambda \in \mathcal{V}_\ell^h$,

$$
\begin{aligned}
& B_f^{VMS}\left(\left\{\mathbf{w}_f^h, q^h\right\}, \left\{\mathbf{u}_f^h, p^h\right\}\right) - F_f^{VMS}\left(\left\{\mathbf{w}_f^h, q^h\right\}\right) + B_s\left(\mathbf{w}_s^h, \mathbf{y}^h\right) - F_s\left(\mathbf{w}_s^h\right) \\
& + \int_{\mathcal{S}^{sh}}\left(\mathbf{w}_f^h - \mathbf{w}_s^{sh,h}\right) \cdot \lambda \mathbf{n}_s^{sh} d\mathcal{S} \\
& + \int_{\mathcal{S}^{sh}} \delta\lambda\left(\left(\mathbf{u}_f^h - \mathbf{u}_s^{sh,h}\right) \cdot \mathbf{n}_s^{sh} - \frac{r}{\beta_{NOR}^{sh}}\lambda\right) d\mathcal{S} \\
& + \int_{\mathcal{S}^{sh}}\left(\mathbf{w}_f^h - \mathbf{w}_s^{sh,h}\right) \cdot \beta_{NOR}^{sh}\left(\left(\mathbf{u}_f^h - \mathbf{u}_s^{sh,h}\right) \cdot \mathbf{n}_s^{sh}\right)\mathbf{n}_s^{sh} d\mathcal{S} \\
& + \int_{\mathcal{S}^{sh}}\left(\mathbf{w}_f^h - \mathbf{w}_s^{sh,h}\right) \cdot \beta_{TAN}^{sh}\left(\left(\mathbf{u}_f^h - \mathbf{u}_s^{sh,h}\right) - \left(\left(\mathbf{u}_f^h - \mathbf{u}_s^{sh,h}\right) \cdot \mathbf{n}_s^{sh}\right)\mathbf{n}_s^{sh}\right) d\mathcal{S} \\
& + \int_{\mathcal{L}^{be}}\left(\mathbf{w}_f^h - \mathbf{w}_s^{be,h}\right) \cdot \beta^{be}\left(\mathbf{u}_f^h - \mathbf{u}_s^{be,h}\right) d\mathcal{L} = 0,
\end{aligned}
\tag{43}
$$

where B_f^{VMS} and F_f^{VMS} are the VMS discretizations of B_f and F_f, respectively, the superscript h denotes the corresponding variable in the discrete space, β^{sh}'s and β^{be} are penalty parameters for fluid–shell and fluid–beam interfaces, respectively, and $r \geq 0$ is a dimensionless constant, typically $\ll 1$. The term associated with r is introduced to regularize the no-penetration constraint in order to circumvent the inf–sup condition (see Kamensky et al. [48] for details); it can be viewed as a degenerate case of strongly-consistent Barbosa–Hughes stabilization [84]. It is important to note here that in Eq. (1), the fluid–structure coupling terms are integrated over Γ_I; we separate these terms and choose Γ_I to be $\mathcal{L}^{be}$ for the fluid–beam term and $\mathcal{S}^{sh}$ for the fluid–shell terms.

2.5. Time integration and solution strategies

Partial derivatives with respect to time in the fluid and structure subproblem formulations are discretized using the generalized-α method [82, 85, 86]. A semi-implicit time integration procedure, where we integrate the fluid–structure penalty coupling implicitly then update the Lagrange multiplier for the no-penetration constraint explicitly, is used to solve the FSI equation system [45, 46]. The procedure can be generalized into two stages. The first stage is to solve implicitly for the $n + 1$ time level fluid, solid structure, mesh displacement, shell structure, and beam structure unknowns, using a combination of quasi-direct and block-iterative coupling strategies [87, 88], holding the Lagrange multiplier fixed at its current value at time level n. For each Newton iteration for solving the nonlinear system of the first stage, we first solve the fluid and solid problems together as a subsystem due to the nature of

their conforming discretizations, then solve the subsequent problems of mesh-moving, shell, and beam subsystems individually. For solving each current subsystem, the most updated solutions obtained from solving previous subsystems are used. The residuals of all the subsystems are converged to some tolerance, before advancing to the next stage.

The second stage is to update the fluid–shell structure interface Lagrange multiplier by adding the normal component of penalty forces derived from the fluid and structure solutions in the first stage. The Lagrange multiplier is represented in the discrete setting by a set of scalars stored at the quadrature points used to compute integrals over $\mathscr{S}^{\text{sh}}$. These scalar samples at time level $n + 1$ are updated explicitly using the formula

$$\lambda^{n + 1} = \lambda^n + \beta_{\text{NOR}}^{\text{sh}} R^{n + \alpha_f}, \tag{44}$$

where $R^{n + \alpha_f}$ is a regularized no-penetration constraint residual

$$R^{n + \alpha_f} = \left(\mathbf{u}_{\text{f}}^{n + \alpha_f} - \left(\mathbf{u}_{\text{s}}^{\text{sh}} \right)^{n + \alpha_f} \right) \cdot \mathbf{n}_{\text{s}}^{\text{sh}} - \frac{r}{\beta_{\text{NOR}}^{\text{sh}}} \lambda^{n + 1}, \tag{45}$$

and $n + \alpha_f$ is an intermediate time level, between steps n and $n + 1$, associated with the generalized-α algorithm. Analysis of stability and accuracy of this methodology, which we refer to as the dynamic augmented Lagrangian approach, can be found in Kamensky et al. [89] and Yu et al. [52].

3. Geometry modeling

In this work, a self-expandable 26 mm Medtronic CoreValve (CV26), as shown in Hopf [90, Figure 2.43], is modeled and studied with the FSI simulation. The CV26 consists of three bioprosthetic leaflets and a skirt sutured onto a tubular nitinol-based frame, and is intended for patients with 20–23 mm annulus diameters. We propose the following geometry modeling strategy to build the structure of the THV and the aorta. First the frame geometry is constructed, and the skirt is built to follow the frame profile. The three CV26 leaflets are then designed based on frame geometry and the attachment edges between the leaflets and the skirt. Finally the aorta is constructed from patient-based data. Detailed procedures for this modeling procedure are described in the following sections to obtain the final CV26 IGA model, shown in Figure 1, and the ascending aorta model.

3.1. Frame

The CV26 frame is laser-cut from a solid tube into 30 individual wires with a total of 165 connection points. These wires are modeled using the extension of the isogeometric Bernoulli beams described in Section 2.3.3, with each beam centerline defined as a cubic NURBS curve (weights are set to 1). Thus, there are two primary steps in the design procedure: defining the centerline NURBS curves and defining the cross-sectional profiles along the curves. In this model, the frame is assumed to be radially symmetric, so it is natural to define cylindrical coordinates, r_c, ϕ_c, and z_c, and the corresponding cylindrical unit vectors, $\hat{r}_c$, $\hat{\phi}_c$ and $\hat{z}_c$, to describe the frame geometry.

The THV frame contains many connected locations between wires; each connection must be modeled correctly to capture the physical behavior of the wires at each connection point. To accomplish this, we first consider that the two wires must intersect at a single physical location that will be shared before and after deformation. As demonstrated in the simple case shown in Figure 2b, only three cubic NURBS basis functions influence each knot location on the defined uniform knot vector (indicated by the red dash on the horizontal axis). Thus, a simple method to connect two cubic NURBS curves at a single point is to define the desired connection point at the physical location of a knot, and to collocate three pairs of corresponding control points from the two curves. As demonstrated in Figure 2a, the physical location associated with the $\xi = 0.5$ knot location is only influenced by control points 3, 4, and 5. By constraining these three control point pairs to move together, the physical location of the single shared point will be maintained throughout the deformation. For other degree NURBS curves, the number of collocated control points should be adjusted appropriately.

The design dimensions of the CV26 considered in this work are estimated according to a given bottom diameter of 26 mm and Figure 2.43 in Hopf [90]. Based on the estimated diameters along the frame profile, a set of baseline key points that define the top, bottom, and connection locations on a single wire are described in the cylindrical coordinate system. Figure 3 shows the diameter profile, the set of initial key points, $\mathbf{P}_1$ to $\mathbf{P}_{11}$, and the table that lists the corresponding cylindrical coordinates of these points. Based on the previous demonstration, the curve geometry is defined so that each connection location will be set at the physical location of a knot, and the required three control points for the connection point are also defined at this location. One additional control point is introduced at each end of the curve to control the shape of the wire. As shown in Figure 3, once the first curve (red curve) is properly defined, a second curve (blue curve) is defined by mirroring the first curve across the $r_c z_c$-plane at $\phi_c = 0$. To maintain the radial symmetry of the frame at connection locations between the pair of wires, each set of control points that correspond to a key point must also be collinearly defined along the z_c-axis. For simplicity, we choose a uniform knot vector so that the central control point in each group of three collinear points will naturally coincide with the connection location. The distance from the connection location to the adjacent collinear control points can then be adjusted to visually match the geometry of the frame shown in Hopf [90, Figure 2.43].

A clamped condition is defined between wires, so we also need to guarantee that the moment will be transferred through the connection point. The following two conditions must be met to ensure the moment transfer at the connection: the tangents at the connection points of both curves must be equal and the angle between the two curves must be maintained. By design, the red wire and the mirrored blue wire in Figure 3 share the same basis functions. Therefore, the first derivatives of the basis functions for these two curves are also identical, which satisfies the equal tangent condition at the connection points. To satisfy the second condition, two control points that are overlapped in an undeformed configuration will be treated as a single control point during the simulation. Therefore, the four degrees of freedom, three translations and one rotation, for the overlapping control points are shared. Thus, the two control points share identical updated solutions, which satisfies the angle

condition between these two curves at the connection points during deformation. With these two conditions fulfilled, the moment can be properly transferred through the connection point.

After the pair of curves is defined, the cross-sectional profiles must also be described. These profiles are defined over the entire NURBS curve using two local unit vectors, $\mathbf{v}_2$, and, $\mathbf{v}_3$. In this work, the following approach is proposed to determine the orientation of these orthogonal base vectors that define the cross-sectional profiles. Let $\mathbf{v}_1$ be the local unit vector that defines the tangent of the curve. Then, define the local unit vector, $\mathbf{v}_2$, to be perpendicular to $\mathbf{v}_1$ and the cylindrical unit vector,

$$\hat{\boldsymbol{\phi}}_c = \begin{pmatrix} -\sin\phi_c \\ \cos\phi_c \\ 0 \end{pmatrix}, \tag{46}$$

and $\mathbf{v}_3$ to be perpendicular to $\mathbf{v}_1$ and $\mathbf{v}_2$. Hence, these two unit vectors representing the crosssectional profile can be defined as

$$\mathbf{v}_2 = \mathbf{v}_1 \times \hat{\boldsymbol{\phi}}_c \tag{47}$$

$$\mathbf{v}_3 = \mathbf{v}_1 \times \mathbf{v}_2. \tag{48}$$

In this work, we define a rectangular cross-section with a constant width of 0.54 mm along $\mathbf{v}_2$ and a constant width of 0.21 mm along $\mathbf{v}_3$ based on the information in Hopf [90]. For the formulation of the Bernoulli beam described in Section 2.3.3, we choose $\mathring{\mathbf{a}}_2$ and $\mathring{\mathbf{a}}_3$ to be $\mathbf{v}_2$ and $\mathbf{v}_3$, respectively.

From the defined curves and cross-sectional profiles, the final frame geometry can then be constructed based on the radial symmetry. As depicted in Figure 4, the two initial wires are repeated radially about the z_c-axis to construct the complete frame.

3.2. Skirt and leaflets

To construct the skirt geometry, we first design the top edge of the skirt to intersect with the modeled frame and to visually match the skirt geometry shown in Hopf [90, Figure 2.43]. With the top edge defined, the rest of the skirt surface should be defined to follow the geometry of the frame; however, this is not a straightforward process. As shown in Figure 5a, an initial skirt design is first constructed using three identical NURBS surfaces (weights are set to 1) that roughly match the geometry of the frame and that are connected with vertical C^0 lines. A penalty-based approach is then employed to force the skirt to conform to the frame geometry by penalizing the current location of the skirt against the reference location of the frame. To achieve this, a shell simulation is performed with the penalty term,

$$+ \int_{\mathscr{L}^{\mathrm{be}}} \alpha'_{\mathrm{sb}} \mathbf{w}_s^{\mathrm{sh}} \cdot \left(\mathbf{x}^{\mathrm{sh}} - \mathring{\mathbf{x}}^{\mathrm{be}} \right) \mathrm{d}\mathscr{L}, \tag{49}$$

added to the structural formulation. At the $C0$ lines, the skirt surfaces are coupled using the shell–shell coupling method described in Section 2.3.4. The final conforming geometry of the skirt, shown in Figure 5b, is used as the reference configuration for the THV simulations. In practice, the initial design of the skirt may be very different from the frame, which makes $\mathbf{x}^{sh} - \mathring{\mathbf{x}}^{be}$ very large. Thus, the required α'_{sb} for this procedure is determined to be 100 times smaller than α_{sb} defined in Section 2.3.4.

Following the leaflet parametric design procedure proposed in Xu et al. [50], the leaflets are defined from a given attachment edge, a free edge, and a curvature. For the THV, the attachment edge of the leaflet is determined by the structure of the frame and the top edge of the skirt. The free edge and the curvature of the leaflet are designed empirically so that the leaflets visually match Hopf [90, Figure 2.43] and Azadani and Tseng [91, Figure 2]. It is not straightforward to directly design the closed shape of leaflet shown in Azadani and Tseng [91, Figure 2]. Therefore, an initial design is first generated, as shown in Figure 6a. A uniform pressure is then applied on the three surfaces to deform the leaflets until the geometry is visually similar to the leaflets in Azadani and Tseng [91, Figure 2]. The rotational penalty described in Section 2.3.4 is neglected in this step since the moment transfer between the leaflets and the skirt is unnecessary during this part of the design process. Figure 6b shows the final geometry of the leaflets that will be used as the reference leaflet configuration for the THV simulations.

The CV26 leaflet design also incorporates three enlarged lateral end regions that form the commissural joints [92]. In this work, these structures are modeled with 6 NURBS surfaces whose initial shape roughly follow the frame geometry. The same penalty technique employed for the skirt geometry is again applied to match the surfaces to the frame. The leaflets are coupled to the skirt and commissural joints at the attachment edges during the THV simulations using the penalty coupling approaches described in Section 2.3.4 to impose the displacement and rotational continuity between shell surfaces.

The computational meshes for the final skirt and leaflet geometries are illustrated in Figure 7. The skirt mesh contains a total of 324 cubic NURBS elements and 567 control points, and the commissural joints contain a total of 72 elements and 270 control points, as shown in Figure 7a. Figure 7b shows the fiber orientation of 45∘ on the leaflet and a total of 1080 elements and 1449 control points for all three leaflets.

3.3. Aorta

The aorta geometry is constructed based on the statistics regarding adult aorta sizes obtained from 2D echocardiographic images [93–95] and is modeled with three main components: the root, base, and tubular ascending aorta. The root is modeled using the same parametrization method described in Morganti et al. [93] and is detailed in Figure 8a. Four key cross sections, defined from the ventriculo-aortic junction, the sinuses of Valsalva, the sinotubular junction, and the tubular ascending aorta, are used to characterize the root. The corresponding diameters of the cross sections are defined as D_A, D_{SV}, D_{STJ}, and D_{TAA}, respectively, as shown in the upper figure of Figure 8a. The clover-shaped cross section is constructed using three circular arcs to represent the three sinuses, with dimensions

illustrated in the lower part of Figure 8a. In this work, all of the α angles are chosen to be 60○. The details of the length scales are listed in Table 1. Note that the annulus diameter is 23 mm therefore CV26 is suitable for this aorta configuration. The four defined cross sections are interpolated using cubic NURBS functions to construct the root surface. The surface tangents at the cross sections of D_{SV}, D_{STJ}, and D_{TAA} are constrained to the vertical direction. The base section is constructed using a circular cylinder with radius D_A that is attached to the bottom of the root. This is used to represent the upper region of the left ventricle. The tubular ascending aorta surface is constructed using circular cross sections and a centerline that are both extracted from patient-specific data. The diameter of the lowest cross section of the tubular ascending aorta is defined to be D_{TAA}, and the surface tangent at the cross section is again constrained to the vertical direction.

The final aorta geometry is used as the lumen surface of the geometry model, which is the interface between the artery wall and fluid domain. The artery wall thickness is defined as 14% of the local lumen radius. The blood flow domain and artery wall are constructed following the workflow detailed in Xu et al. [50], and quadratic trivariate NURBS elements are used to discretize the entire domain. Figure 8b illustrates the computational mesh, with 88,560 elements in the fluid domain, and 8640 elements in the artery wall. In this work, we refer to the *inlet* as the left ventricle end of the artery and the *outlet* as the tubular ascending aorta end.

4. Application to FSI analysis of TAVR

In this section, we apply the developed immersogeometric framework to the FSI simulation of the THV. We first validate the implementation of the beam formulation using a number of example problems. We also simulate the THV crimping process and check the fluid–beam interaction. Finally, we simulate and analyze the full TAVR process using FSI.

4.1. Frame validation

To ensure the correct implementation of the Bernoulli beam, we apply our method to a well-established benchmark problem, the nonlinear analysis of a 45○-bending beam [96–99]. We also test the effectiveness of the method to model the connection points between two beams using a simple example problem. Finally, we perform a tension test on the CV26 frame model and compare the simulation results to experimental results to validate the effectiveness of the proposed technology.

4.1.1. Geometrically-nonlinear beam benchmark—The beam geometry considered in the first benchmark problem is a circular segment with radius $R = 100$ m and a square cross-sectional profile with an area of 1 m^2. A clamped boundary condition is applied at one end of the beam, and a point load F is applied out-of-plane at the other end. The Young's modulus of the beam is $E = 100$ GPa, the Poisson's ratio is $\nu = 0.0$, and the point load is determined by a load parameter $k = \frac{FR^2}{EI}$, where I is the moment of inertia of the cross-section for the beam. The deflections are non-dimensionalized by the radius R. The problem setup and simulation of a cubic NURBS curve with 16 elements at $k = 5$ are shown in Figure 9a. In Figure 9b, the non-dimensional tip displacements are compared to the results in Bathe

and Bolourchi [96]. For comparison, the results of the non-dimensional z-deflection from the linear analysis are also included. The simulated deflections are in excellent agreement with the reference solutions.

4.1.2. Connection point problem—To test the new technology proposed for the connection points, an example problem is performed with a mesh independence study. The centerline of the first beam (shown in Figure 10) is constructed using a cubic NURBS curve (weights are set to 1) with 7 control points, listed in Table 2, and a uniform knot vector. The first beam is defined with a rectangular cross section of width 100 mm and height 30 mm, with the height oriented in the z-direction. The second beam is then generated by duplicating and rotating the first beam by 120○ about the y-axis, as shown in Figure 10b. Control points $\mathbf{Q}_3$, $\mathbf{Q}_4$, and $\mathbf{Q}_5$ are overlapped with the corresponding three control points of the second beam to define a connection point. A clamped boundary condition is applied at one end of the first beam, as shown in Figure 10a, which means all degrees of freedom on control points $\mathbf{Q}_6$ and $\mathbf{Q}_7$ are fixed during the simulations. A force F is applied to the end of the other beam in the $-x$-direction. If the force is transferred properly through the connection point, the entire structure will deform. The displacement in the z-direction of control point $\mathbf{Q}_1$ is collected. The Young's modulus and Poisson's ratio are set to $E = 100$ MPa and $\nu = 0.33$, respectively. These mechanical properties are chosen such that the displacement is clearly visible. A frame from the simulation result is plotted in Figure 11.

The results from a global h-refinement study are shown in Figure 12a. Global h-refinement of the beams shows converged results around three levels of refinement, however, this refinement procedure is very computationally expensive. Based on our observation of the deformed frame structure, the connection points show a larger local change in curvature compared to the rest of the structure. Therefore, instead of global h-refinement, we propose a different way to perform h-refinement, which focuses on the connection points, called local h-refinement. Refinement around the connection points is also important to limit the effect of the clamped boundary condition in a localized region. The new local refinement is performed on the globally-refined M2. The locally refined meshes are denoted starting from the first refinement level as M2L1 to M2L3, with the corresponding number of elements shown in Table 3. At each successive level of local refinement, the elements directly adjacent to the connection points are divided into two elements, as shown in Figure 13. The results using local h-refinement are shown in Figure 12b, which demonstrates that performing local refinement obtains similar results to global h-refinement with significantly fewer elements.

4.1.3. Frame tension test—To further validate the new technology proposed for the frame geometry, we perform a two-point tension test of the frame and compare the computed results to the experimental and simulation results performed in Hopf [90]. For the experiment, two points at the top of the frame are attached to thin steel wires, which are clamped and pulled by a biaxial machine as shown in Hopf [90, Figure 2.58]. To simulate this procedure, two opposing forces in the horizontal direction are applied to opposite points on the frame, as shown in Figure 14. The St. Venant–Kirchhoff material model is applied with Young's modulus of $E = 58$ GPa and Poisson's ratio of $\nu = 0.33$, as reported in Hopf

[90]. The change of distance between the two points with opposing forces is collected and a mesh independence study is performed.

The original frame discretization indicated in Section 3.1 consists of 840 elements, denoted as M0. Global h-refinements are performed and labeled as M1 to M4, with the corresponding number of elements shown in Table 4. The results of the tension tests with global h-refinement are shown in Figure 15a. The refinements M3 and M4 give similar results that are qualitatively close to the experimental and simulation results reported in Hopf [90]. Note that the exact material properties of the frame are not known, which can contribute to the discrepancy from the experimental data. Local h-refinements from the globally-refined M1 at the connection locations are also performed and labeled as M1L1 to M1L3. The corresponding number of elements is listed in Table 4. The results of this local h-refinement study are shown in Figure 15b. In comparison to global h-refinement, the local refinement gives similar results with a significantly lower number of elements, decreasing the computational cost substantially. Thus, we select local h-refinement M1L2 for the FSI simulations.

4.2. TAVR FSI simulation setup

Transcatheter heart valves are designed to be oversized with respect to the diameter of the aortic annulus. In this work, the diameter of the CV26 THV is larger than the diameter of the artery, as described in Section 3. The whole THV needs to be crimped enough to fit inside the artery and then deployed at a specific location. We create a crimping and deployment procedure to realistically model the interaction between the THV and the aortic wall[4]. Consequently, before setting up the complete FSI simulation, there are two main stages of simulation that need to be performed. The first stage is to crimp the THV model and the second stage is to deploy it into the deformable artery.

4.2.1. THV crimping—The crimping procedure for the THV is a pure structural simulation. The frame is modeled using the St. Venant–Kirchhoff material model with Young's modulus of $E = 58$ GPa and Poisson's ratio of $\nu = 0.33$, as reported in Hopf [90]. The mass density of the frame is set to 6.45 g/cm^3. According to Bruschi et al. [100], the CV26 is a tri-leaflet porcine pericardial tissue valve. In this work, the leaflets are modeled using the Lee–Sacks anisotropic material model described in Section 2.3.2. The material fitting procedure proposed in Wu et al. [51] is used to obtain the parameters for the Lee–Sacks material model based on the 0∘-fiber biaxial mechanical properties of porcine pericardium reported in Caballero et al. [101]. The fitting results for the leaflets are shown in Figure 16a with the obtained parameters $c_0 = 117.1375$ kPa, $c_1 = 41.4347$ kPa, $c_2 = 109.7423$, $c_3 = 132.4545$, and $\delta = 0.9883$. In this work, we assume a fiber orientation of 45∘ for the leaflets, as shown in Figure 7b, based on the fiber orientation of native porcine valves observed in Mega et al. [102]. The fiber orientation of the skirt is unclear; for simplicity, the skirt is modeled using the Lee–Sacks isotropic material model. The fitting result for the skirt is shown in Figure 16b, with obtained parameters $c_0 = 117.1375$ kPa, $c_1 = 60.3991$ kPa, $c_2 =$

---

[4]We note that we do not consider the procedure of crimping the THV into a catheter. Such a procedure requires the modeling of shape memory and superelastic properties of the nitinol frame, which is outside the scope of this work.

92.4784, and $\delta = 1$. Based on the discussions from Bruschi et al. [100], the thickness of the skirt and leaflets is set to 0.033 cm. The mass densities of these components are set to 1.0 g/cm^3.

To crimp the THV, a radially inward force that is nonuniform along the vertical length of the frame is applied. Since the wires are more concentrated in the lower region of the frame and this area is also coupled to the skirt and leaflets, the lower region of the THV crimps more slowly than the upper region when the same magnitude of force is applied. Thus, in order to avoid over crimping the topmost region, we apply a nonuniform force with a higher magnitude on the lower part of the frame. This force is applied on the beam until the THV is sufficiently crimped so that the diameter of the crimped THV is less than the diameter of the aortic annulus, as shown in Figure 17a. During this simulation we consider only the radial components of the acceleration, velocity, and displacement for each of the lowermost control points of the beam, which constrains these control points to move only in the radial direction.

4.2.2. THV deployment—In practice, the THV is deployed into the artery in conjunction with the blood flow, so we choose to replicate this process by using FSI for the deployment simulation. To obtain the prescribed artery wall prestress that is required for FSI simulations, we apply the left ventricular pressure at peak systole[5] ($t = 0.25$ s) at the inlet of the artery and a resistance boundary condition at the outlet. The resistance boundary condition is applied as the traction, $-(p_0 + RQ)\mathbf{n}_f$, where $p_0 = 80$ mmHg is a constant physiological pressure level, $R = 70$ (dyn s)/cm^5 is a resistance constant, Q is the volumetric flow rate through the outlet, and $\mathbf{n}_f$ is the outward facing normal of the fluid domain as shown in Figure 8b. The fluid density and viscosity are $\rho_f = 1.0$ g/cm^3 and $\mu_f = 3.0 \times 10^{-2}$ g/(cm s), respectively, which model the physical properties of human blood. The backflow stabilization with $\gamma = 0.5$ is applied at both the inlet and outlet. This simulation is used to obtain $\widetilde{\mathbf{h}}_f$ in Eq. (8); the prestress tensor $\mathbf{S}_0$ is then computed following the procedure in Xu et al. [50]. The same fluid properties, resistance boundary condition, and backflow stabilization are applied for all the FSI simulations in this work.

During the FSI deployment simulation, the crimped THV is immersed into a pressure-driven incompressible flow through a deformable artery. The pressure at $t = 0.6$ s in Figure 18 is applied as a traction boundary condition at the inlet. We choose to deploy the THV during diastole which causes the valve to close and the fluid to reach a hydrostatic state, while the system reaches a quasi-static state. The artery wall is modeled as a neo-Hookean material with dilational penalty as discussed in Section 2.3.1, where the shear and bulk moduli of the model are selected to produce a Young's modulus of 1.0 MPa and Poisson's ratio of 0.45. The density of the arterial wall is 1.0 g/cm^3, and the motion of the solid structure is damped by a body force with a damping coefficient of 1.0×10^4 s^{-1} to model the interaction of the artery with the surrounding tissues and interstitial fluid. The inlet and outlet cross sections are free to slide in their tangential planes and deform radially, but they are constrained not to

---

[5]The CV26 THV modeled in this work is suggested for use in a 20 mm to 23 mm diameter aortic annulus. As shown in Table 1, the aortic annulus for the artery used here has a 23 mm diameter. Hence, we choose to build the prestress based on conditions of the fully expanded state during the cardiac cycle, which occurs at peak systole.

move in the normal directions [60]. The penalty parameters for the fluid–shell and fluid–beam[6] coupling in Eq. (43) are set to $\beta_{\text{TAN}}^{\text{sh}} = 2.0 \times 10^2 \text{g}/(\text{cm}^2\,\text{s})$, $\beta_{\text{NOR}}^{\text{sh}} = 2.0 \times 10^3 \text{g}/(\text{cm}^2\,\text{s})$, and $\beta^{\text{be}} = 2.0 \times 10^2$ g/(cm s) and the parameters for the contact problem in Eq. (39) are presented in Table 5.

During the deployment simulation, the control points in the ring associated with $\mathbf{P}_9$ in Figure 3 are constrained in the vertical direction to maintain the location within the artery. This particular ring is chosen to ensure that the attachment edge of each leaflet is aligned to the corresponding sinus. The nonuniform force applied on the THV during crimping is then gradually released to allow the THV to expand and fit into the artery, as shown in Figure 17b. Once the THV model is fully deployed into the deformable artery at a target location, we define this state as the deployed configuration, which is used for the calculation of friction. This configuration also provides the initial conditions for the full FSI cardiac cycle simulation.

Remark 1. After deployment, the THV does not return to its reference configuration; as a result, prestrain is introduced on the THV before the FSI simulation. Figure 17b shows the deployed configuration during diastole. The leaflets in this configuration are fully loaded and have a maximum strain of 0.201. However, this strain obtained using FSI simulation could very well be dominated by the loading of the blood pressure. To examine the prestrain on the THV solely due to the deployment, we repeat the simulation and remove the coupling between the fluid and the THV structure.

Figure 17c shows the strain introduced without the interaction with the fluid. The maximum strain on the leaflets in this configuration is 0.068.

4.3. FSI simulation results and discussion

For the FSI simulation, a physiologically-realistic left ventricular pressure profile shown in Figure 18 is applied as a traction boundary condition at the inlet. The duration of a single cardiac cycle is 0.86 s and the time step size is set to $\Delta t = 1.0 \times 10^{-4}$ s. The starting point of the FSI simulation is at time $t = 0.6$ in order to be consistent with the deployment simulation. Three cardiac cycles are computed, and the final cycle is used for the remainder of the discussion. Figure 19 shows several snapshots of the detailed fluid solution fields, strain maps, and the top view of CV26 during the cardiac cycle. During systole, starting at $t = 0.0$ s, the inlet pressure is larger than the outlet pressure (see Figure 18), which causes the valve to open and the strain to start increasing. At $t = 0.06$ s, the leaflets open and contact the frame. The valve fully opens at $t = 0.25$ s. The valve starts to close and reaches the fully closed configuration around $t = 0.38$ s. The fully loaded configuration at $t = 0.52$ s is shown with a maximum strain of approximately 0.201. The strain map for the leaflets on both the inner and outer surfaces are plotted during peak systole and peak diastole in Figure 20. Generally, the highest level of strain occurs during diastole when the leaflets are fully loaded. In this work we have a strain level of about 0.201 during diastole. However, it is observed that the inner side of the leaflet during systole also has a large maximum strain

---

[6]A simple study to determine the effectiveness of the penalty coupling for the fluid–beam problem is shown in Appendix A.

value, at about 0.195. This large strain level occurs due to the curvature of the leaflets in the fully open configuration.

The total radial and static friction forces are plotted over a single cardiac cycle in Figure 21. The variation of the radial force on the CV26 is mainly due to the interaction between the frame and the deformable artery wall. As depicted in Figure 21a, the radial force drops during systole (approximately from $t = 0.0$ s to $t = 0.3$ s) because the artery wall expands due to the pressure of blood flow. When the blood flow slows down during diastole (from approximately $t = 0.3$ s to $t = 0.86$ s), the artery wall shrinks, which increases the radial force on the CV26.

The friction force is separated into the x-, y-, and z-components and shown in Figure 21b. The role of the friction force is to maintain the location of the THV while the forces from the blood flow act on it. Based on the results, the x- and y-components of the friction force are negligible compared to the z-component, so we consider only the z-component for the following discussion. The positive direction of the friction force is defined to be in the positive z-direction. Thus, during systole, the friction force is negative while the blood flow provides positive forces. During diastole, the blood flow provides negative forces as the valve closes, causing the friction force to become positive. The friction force magnitude distribution is shown in Figure 22 for the fully open and fully closed configurations. In the fully closed configuration, the magnitude of the friction force is significantly larger compared to the fully opened configuration, especially around the annulus. As the valve closes and the leaflets provide a blockage for the blood flow, the magnitude of the friction force increases to counter the effect of the additional force on the THV.

Figure 23 shows the ratio of friction force magnitude to radial force magnitude. The maximum value of this ratio over a cycle is about 0.22. The friction force, F_{fri}, and radial force, F_{rad}, may be related by the equation, $F_{\mathrm{fri}} \quad \mu F_{\mathrm{rad}}$, where μ is the coefficient of friction. Equality only occurs at the maximum friction force before the objects begin to slide. Based on experiments performed by Mummert et al. [104], the coefficient of friction between the artery wall and the THV frame is approximately 0.10 ± 0.01. The calculated ratio of friction force to radial force in this work is higher than 0.10 during diastole, so the THV will not remain stationary in the artery in the existing configuration. To lower this ratio, one may elect to increase the diameter of the THV frame in order to increase the radial force, or change aspects of the geometry design to decrease the friction force. The results obtained using the proposed immersogeometric FSI framework provide valuable information that can be used to study the anchoring ability of the THV under physiologically realistic conditions.

5. Conclusions

In this paper, an immersogeometric framework for the FSI simulation of TAVR is successfully developed. Methods are proposed to model and couple the main components involved in the TAVR procedure, including the interactions among the artery wall, leaflets and skirt, frame, and blood flow. The THV frame is parametrically modeled and validated; a parameterized design of the entire THV is then simulated and analyzed using the proposed immersogeometric framework. The simulation is comprised of three main stages to create a

physiologically realistic and meaningful simulation: crimping, deployment, and the FSI simulation. The crimping stage is necessary to deploy the THV, as it is designed to be larger than the artery. The deployment procedure allows us to account for the interaction between the THV and artery wall as the THV expands. During the FSI simulation, radial and friction forces are computed and studied simultaneously to obtain the ratio of friction force to radial force, which is important for indicating the anchoring capability of the THV. By comparing the computed values to the given coefficient of friction, changes may be made to the THV geometry to lower the risk of migration.

While the static friction formulation is sufficient for the objectives of this study, the simplicity of the model leads to limitations that we may address in future work. The static friction only allows us to study the anchoring ability and estimate the likelihood of migration. Including a dynamic friction formulation would allow us to study the behavior of the THV migration over the cardiac cycle. The St. Venant–Kirchhoff material model used for the frame presents another limitation as it does not accurately reflect the shape memory and superelastic properties of the nitinol frame. In this work, we only crimp the THV enough to fit within the artery, so an elastic model is sufficient; however, a superelastic model would be necessary in order to fully crimp the THV to fit into a catheter. The penalty method used for fluid–beam coupling also introduces some limitations. The penalty parameter and mesh resolution must be carefully chosen in order to accurately capture the interaction between the fluid and the frame. Alternatively, one may elect to use the line drag method (see, e.g., Tezduyar et al. [105] and Takizawa and Tezduyar [106]), which uses the relative velocity and empirical approximation of drag over cylinders to compute the drag force applied to the line by the fluid. However, since the frame is coupled to the shell structures on the bottom most portion of the THV, this method would mainly only be needed for the top portion where the fluid flows over the frame.

In the future, we plan to couple the proposed TAVR FSI framework with patient-specific information to determine the possibility of migration. This combination can provide valuable information for clinical planning and decision making in determining the correct sizing for the THV. If joined to a derivative-free optimization algorithm as in Wu et al. [107], such a framework even opens the door for automatic determination of the best choice of THVs using FSI analysis.

Acknowledgments

Appendix A.: Fluid–beam interaction

To assess the technology proposed for the interaction between the fluid and the THV, we perform two test cases. The first test case is to study the implementation of the fluid–beam interaction subproblem. The frame, without the leaflets and skirt, is placed in the

deployment location within the artery. The same boundary conditions as discussed in Section 4.2 are applied. To clearly show that the frame interacts with the fluid, friction between the frame and artery wall is not considered so that the frame may move freely inside of the artery. Figure A.1a shows the results obtained at peak systole ($t = 0.22$ s) synchronized with Figure 18. It can be seen that the frame gets pushed through the artery by the pressure of the blood flow, showing the full interaction between the frame and the fluid. The second test case is used to study the interaction between the fluid and the full THV. The full THV is deployed into the deformable artery, again with no friction applied and the same boundary conditions discussed in Section 4.2 are applied. Figure A.1b shows the THV displacement from its original location due to the pressure from the blood flow and lack of friction to hold it in place.

(a) Fluid–frame interaction (b) Fluid–THV interaction
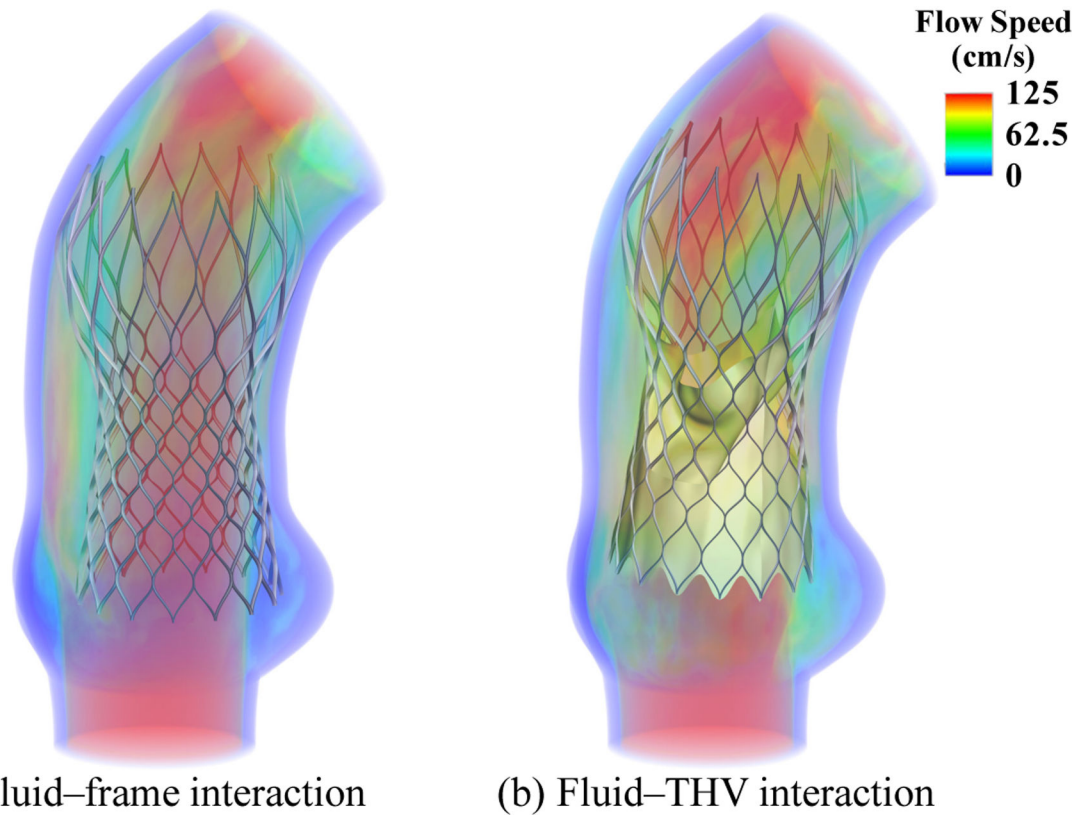
Figure A.1:
FSI simulation of the frame and the THV without friction.

References

[1]. Osnabrugge RLJ, Mylotte D, Head SJ, Van Mieghem NM, Nkomo VT, LeReun CM, Bogers AJJC, Piazza N, and Kappetein AP Aortic stenosis in the elderly. Journal of the American College of Cardiology, 62(11):1002–1012, 2013. [PubMed: 23727214]

[2]. Go AS, Mozaffarian D, Roger VL, Benjamin EJ, Berry JD, Blaha MJ, and et al. Heart disease and stroke statistics–2014 update: A report from the American Heart Association. Circulation, 129(3):e28–e292, 2013. [PubMed: 24352519]

[3]. Schoen FJ and Levy RJ Tissue heart valves: Current challenges and future research perspectives. Journal of Biomedical Materials Research, 47(4):439–465, 1999. [PubMed: 10497280]

[4]. Schoen FJ and Levy RJ Calcification of tissue heart valve substitutes: Progress toward understanding and prevention. The Annals of Thoracic Surgery, 79(3):1072–1080, 2005. [PubMed: 15734452]

[5]. Schoen FJ Cardiac valves and valvular pathology: Update on function, disease, repair, and replacement. Cardiovascular Pathology, 14(4):189–194, 2005. [PubMed: 16009317]

[6]. Schoen FJ Evolving concepts of cardiac valve dynamics: The continuum of development, functional structure, pathobiology, and tissue engineering. Circulation, 118(18):1864–1880, 2008. [PubMed: 18955677]

[7]. Thubrikar MJ, Deck JD, Aouad J, and Nolan SP Role of mechanical stress in calcification of aortic bioprosthetic valves. The Journal of Thoracic and Cardiovascular Surgery, 86:115–125, 1983. [PubMed: 6865456]

[8]. Vesely I, Barber JE, and Ratliff NB Tissue damage and calcification may be independent mechanisms of bioprosthetic heart valve failure. The Journal of Heart Valve Disease, 10(4): 471–477, 2001. [PubMed: 11499593]

[9]. Sacks MS and Schoen FJ Collagen fiber disruption occurs independent of calcification in clinically explanted bioprosthetic heart valves. Journal of Biomedical Materials Research, 62(3):359–371, 2002. [PubMed: 12209921]

[10]. Siddiqui RF, Abraham JR, and Butany J Bioprosthetic heart valves: Modes of failure. Histopathology, 55:135–144, 2009. [PubMed: 19694820]

[11]. Guidoin R, Douville Y, Clavel M-A, Zhang Z, Nutley M, Pibarot P, and Dionne G The marvel of percutaneous cardiovascular devices in the elderly. Annals of the New York Academy of Sciences, 1197(1):188–199, 2010. [PubMed: 20536849]

[12]. Willson AB, Webb JG, LaBounty TM, Achenbach S, Moss R, Wheeler M, Thompson C, Min JK, Gurvitch R, Norgaard BL, and Hague CJ Three-dimensional aortic annular assessment by multidetector computed tomography predicts moderate or severe paravalvular regurgitation after transcatheter aortic valve replacement: A multicenter retrospective analysis. Journal of the American College of Cardiology, 59(14):1287–1294, 2012. [PubMed: 22365423]

[13]. Pasic M, Unbehaun A, Dreysse S, Buz S, Drews T, Kukucka M, D'ancona G, Seifert B, and Hetzer R Rupture of the device landing zone during transcatheter aortic valve implantation: A life-threatening but treatable complication. Circulation: Cardiovascular Interventions, 5(3):424–432, 2012. [PubMed: 22589295]

[14]. Barbanti M, Yang T-H, Rodès Cabau J, Tamburino C, Wood DA, Jilaihawi H, Blanke P, Makkar RR, Latib A, Colombo A, and Tarantini G Anatomical and procedural features associated with aortic root rupture during balloon-expandable transcatheter aortic valve replacement. Circulation, 128(3):244–253, 2013. [PubMed: 23748467]

[15]. Sinning J-M, Vasa-Nicotera M, Chin D, Hammerstingl C, Ghanem A, Bence J, Kovac J, Grube E, Nickenig G, and Werner N Evaluation and management of paravalvular aortic regurgitation after transcatheter aortic valve replacement. Journal of the American College of Cardiology, 62(1):11–20, 2013. [PubMed: 23644081]

[16]. Goldenberg G, Kusniec J, Kadmon E, Golovchiner G, Zabarsky R, Nevzorov R, Vaknin H, Assali A, Kornowski R, Haim M, and Strasberg B. Pacemaker implantation after transcatheter aortic valve implantation. The American Journal of Cardiology, 112(10): 1632–1634, 2013. [PubMed: 23998348]

[17]. Tan JS, Leipsic J, Perlman G, Stub D, Dvir D, Hansson NC, Norgaard BL, Blanke P, Cheung A, Ye J, and Thompson CR A strategy of underexpansion and ad hoc post-dilation of balloon-expandable transcatheter aortic valves in patients at risk of annular injury: favorable mid-term outcomes. JACC: Cardiovascular Interventions, 8(13): 1727–1732, 2015. [PubMed: 26476612]

[18]. Dètaint D, Lepage L, Himbert D, Brochet E, Messika-Zeitoun D, Iung B, and Vahanian A Determinants of significant paravalvular regurgitation after transcatheter aortic valve implantation: Impact of device and annulus discongruence. JACC: Cardiovascular Interventions, 2(9):821–827, 2009. [PubMed: 19778769]

[19]. Ussia GP, Barbanti M, and Tamburino C Management of percutaneous self-expanding bioprosthesis migration. Clinical Research in Cardiology, 99(10):673–676, 2010. [PubMed: 20617324]

[20]. Padala M, Sarin EL, Willis P, Babaliaros V, Block P, Guyton RA, and Thourani VH An engineering review of transcatheter aortic valve technologies. Cardiovascular Engineering and Technology, 1(1):77–87, 2010.

[21]. Mylotte D, Martucci G, and Piazza N Patient selection for transcatheter aortic valve implantation: an interventional cardiology perspective. Annals of Cardiothoracic Surgery, 1(2):206–215, 2012. [PubMed: 23977496]

[22]. Cao C, Ang SC, Vallely MP, Ng M, Adams M, and Wilson M Migration of the transcatheter valve into the left ventricle. Annals of Cardiothoracic Surgery, 1(2):243–244, 2012. [PubMed: 23977502]

[23]. Lerakis S, Hayek SS, and Douglas PS Paravalvular aortic leak after transcatheter aortic valve replacement: Current knowledge. Circulation, 127(3):397–407, 2013. [PubMed: 23339094]

[24]. Athappan G, Patvardhan E, Tuzcu EM, Svensson LG, Lemos PA, Fraccaro C, Tarantini G, Sinning J-M, Nickenig G, Capodanno D, Tamburino C, Latib A, Colombo A, and Kapadia SR Incidence, predictors, and outcomes of aortic regurgitation after transcatheter aortic valve

replacement: meta-analysis and systematic review of literature. Journal of the American College of Cardiology, 61(15):1585–1595, 2013. [PubMed: 23500308]

[25]. O'Sullivan KE, Gough A, Segurado R, Barry M, Sugrue D, and Hurley J Is valve choice a significant determinant of paravalular leak post-transcatheter aortic valve implantation? A systematic review and meta-analysis. European Journal of Cardio-thoracic Surgery, 45(5):826–833, 2013. [PubMed: 24186923]

[26]. Zamorano JL, Gonçalves A, and Lang R Imaging to select and guide transcatheter aortic valve implantation. European Heart Journal, 35(24):1578–1587, 2014. [PubMed: 24459198]

[27]. Borghi A, Murphy O, Bahmanyar R, and McLeod C Effect of stent radial force on stress pattern after deployment: a finite element study. Journal of Materials Engineering and Performance, 23(7):2599–2605, 2014. [PubMed: 25089084]

[28]. U.S. Department of Health and Human Services, Food and Drug Administration. Guidance for industry and FDA staff: Non-clinical tests and recommended labeling for intravascular stents and associated delivery systems, 4 2010.

[29]. Auricchio F, Conti M, Morganti S, and Reali A Simulation of transcatheter aortic valve implantation: a patient-specific finite element approach. Computer Methods in Biomechanics and Biomedical Engineering, 17(12):1347–1357, 2014. [PubMed: 23402555]

[30]. Morganti S, Conti M, Aiello M, Valentini A, Mazzola A, Reali A, and Auricchio F Simulation of transcatheter aortic valve implantation through patient-specific finite element analysis: two clinical cases. Journal of Biomechanics, 47(11):2547–2555, 2014. [PubMed: 24998989]

[31]. Morganti S, Brambilla N, Petronio AS, Reali A, Bedogni F, and Auricchio F Prediction of patient-specific post-operative outcomes of TAVI procedure: the impact of the positioning strategy on valve performance. Journal of Biomechanics, 49(12):2513–2519, 2016. [PubMed: 26748728]

[32]. Ovcharenko EA, Klyshnikov KU, Yuzhalin AE, Savrasov GV, Kokov AN, Batranin AV, Ganyukov VI, and Kudryavtseva YA Modeling of transcatheter aortic valve replacement: Patient specific vs general approaches based on finite element analysis. Computers in Biology and Medicine, 69:29–36, 2016. [PubMed: 26708469]

[33]. Sturla F, Ronzoni M, Vitali M, Dimasi A, Vismara R, Preston-Maher G, Burriesci G, Votta E, and Redaelli A Impact of different aortic valve calcification patterns on the outcome of transcatheter aortic valve implantation: a finite element study. Journal of Biomechanics, 49(12):2520–2530, 2016. [PubMed: 27059259]

[34]. Finotello A, Morganti S, and Auricchio F Finite element analysis of TAVI: Impact of native aortic root computational modeling strategies on simulation outcomes. Medical Engineering & Physics, 47:2–12, 2017. [PubMed: 28728867]

[35]. Mao W, Wang Q, Kodali S, and Sun W Numerical parametric study of paravalvular leak following a transcatheter aortic valve deployment into a patient-specific aortic root. Journal of Biomechanical Engineering, 140(10):101007–11, 2018.

[36]. Bianchi M, Marom G, Ghosh RP, Rotman OM, Parikh P, Gruberg L, and Bluestein D Patient-specific simulation of transcatheter aortic valve replacement: impact of deployment options on paravalvular leakage. Biomechanics and Modeling in Mechanobiology, 18(2): 435–451, 2019. [PubMed: 30460623]

[37]. Kandail HS, Trivedi SD, Shaikh AC, Bajwa TK, Daniel PO, Jahangir A, and LaDisa JF Jr. Impact of annular and supra-annular corevalve deployment locations on aortic and coronary artery hemodynamics. Journal of the Mechanical Behavior of Biomedical Materials, 86:131–142, 2018. [PubMed: 29986288]

[38]. Wu W, Pott D, Mazza B, Sironi T, Dordoni E, Chiastra C, Petrini L, Pennati G, Dubini G, Steinseifer U, Sonntag S, Kuetting M, and Migliavacca F Fluid–structure interaction model of a percutaneous aortic valve: comparison with an in vitro test and feasibility study in a patient-specific case. Annals of Biomedical Engineering, 44(2):590–603, 2016. [PubMed: 26294009]

[39]. Ghosh RP, Marom G, Rotman OM, Slepian MJ, Prabhakar S, Horner M, and Bluestein D Comparative fluid–structure interaction analysis of polymeric transcatheter and surgical aortic valves' hemodynamics and structural mechanics. Journal of Biomechanical Engineering, 140(12):121002–10, 2018.

[40]. Tzamtzis S, Viquerat J, Yap J, Mullen MJ, and Burriesci G Numerical analysis of the radial force produced by the Medtronic-CoreValve and Edwards-SAPIEN after transcatheter aortic valve implantation (TAVI). Medical Engineering & Physics, 35(1):125–130, 2013. [PubMed: 22640661]

[41]. Egron S, Fujita B, Gullón L, Pott D, Schmitz-Rode T, Ensminger S, and Steinseifer U Radial force: an underestimated parameter in oversizing transcatheter aortic valve replacement prostheses: in vitro analysis with five commercialized valves. ASAIO Journal, 64(4): 536–543, 2018. [PubMed: 28885378]

[42]. Cabrera MS, Oomens CWJ, and Baaijens FPT Understanding the requirements of self-expandable stents for heart valve replacement: Radial force, hoop force and equilibrium. Journal of the Mechanical Behavior of Biomedical Materials, 68:252–264, 2017. [PubMed: 28219851]

[43]. Hsu M-C, Wang C, Herrema AJ, Schillinger D, Ghoshal A, and Bazilevs Y An interactive geometry modeling and parametric design platform for isogeometric analysis. Computers and Mathematics with Applications, 70:1481–1500, 2015.

[44]. Herrema AJ, Wiese NM, Darling CN, Ganapathysubramanian B, Krishnamurthy A, and Hsu M-C A framework for parametric design optimization using isogeometric analysis. Computer Methods in Applied Mechanics and Engineering, 316:944–965, 2017.

[45]. Kamensky D, Hsu M-C, Schillinger D, Evans JA, Aggarwal A, Bazilevs Y, Sacks MS, and Hughes TJR An immersogeometric variational framework for fluid–structure interaction: Application to bioprosthetic heart valves. Computer Methods in Applied Mechanics and Engineering, 284:1005–1053, 2015. [PubMed: 25541566]

[46]. Hsu M-C, Kamensky D, Bazilevs Y, Sacks MS, and Hughes TJR Fluid–structure interaction analysis of bioprosthetic heart valves: significance of arterial wall deformation. Computational Mechanics, 54:1055–1071, 2014. [PubMed: 25580046]

[47]. Hsu M-C, Kamensky D, Xu F, Kiendl J, Wang C, Wu MCH, Mineroff J, Reali A, Bazilevs Y, and Sacks MS Dynamic and fluid–structure interaction simulations of bioprosthetic heart valves using parametric design with T-splines and Fung-type material models. Computational Mechanics, 55:1211–1225, 2015. [PubMed: 26392645]

[48]. Kamensky D, Evans JA, and Hsu M-C Stability and conservation properties of collocated constraints in immersogeometric fluid-thin structure interaction analysis. Communications in Computational Physics, 18:1147–1180, 2015.

[49]. Kamensky D, Evans JA, Hsu M-C, and Bazilevs Y Projection-based stabilization of interface Lagrange multipliers in immersogeometric fluid–thin structure interaction analysis, with application to heart valve modeling. Computers and Mathematics with Applications, 74(9):2068–2088, 2017. [PubMed: 29225420]

[50]. Xu F, Morganti S, Zakerzadeh R, Kamensky D, Auricchio F, Reali A, Hughes TJR, Sacks MS, and Hsu M-C A framework for designing patient-specific bioprosthetic heart valves using immersogeometric fluid–structure interaction analysis. International Journal for Numerical Methods in Biomedical Engineering, 34(4):e2938, 2018. [PubMed: 29119728]

[51]. Wu MCH, Zakerzadeh R, Kamensky D, Kiendl J, Sacks MS, and Hsu M-C An anisotropic constitutive model for immersogeometric fluid–structure interaction analysis of bioprosthetic heart valves. Journal of Biomechanics, 74:23–31, 2018. [PubMed: 29735263]

[52]. Yu Y, Kamensky D, Hsu M-C, Lu XY, Bazilevs Y, and Hughes TJR Error estimates for projection-based dynamic augmented Lagrangian boundary condition enforcement, with application to fluid–structure interaction. Mathematical Models and Methods in Applied Sciences, 28(12):2457–2509, 2018.

[53]. Hsu M-C and Kamensky D Immersogeometric analysis of bioprosthetic heart valves, using the dynamic augmented Lagrangian method. In Tezduyar TE, editor, Frontiers in Computational Fluid–Structure Interaction and Flow Simulation, pages 167–212. Springer International Publishing, Cham, 2018.

[54]. Bauer AM, Breitenberger M, Philipp B, Wüchner R, and Bletzinger K-U Nonlinear isogeometric spatial Bernoulli beam. Computer Methods in Applied Mechanics and Engineering, 303:101–127, 2016.

[55]. Herrema AJ, Johnson EL, Proserpio D, Wu MCH, Kiendl J, and Hsu M-C Penalty coupling of non-matching isogeometric Kirchhoff–Love shell patches with application to composite wind turbine blades. Computer Methods in Applied Mechanics and Engineering, 346:810–840, 2019.

[56]. Bazilevs Y, Hsu M-C, and Scott MA Isogeometric fluid–structure interaction analysis with emphasis on non-matching discretizations, and with application to wind turbines. Computer Methods in Applied Mechanics and Engineering, 249:28–41, 2012.

[57]. Hughes TJR, Liu WK, and Zimmermann TK Lagrangian–Eulerian finite element formulation for incompressible viscous flows. Computer Methods in Applied Mechanics and Engineering, 29:329–349, 1981.

[58]. Esmaily-Moghadam M, Bazilevs Y, Hsia T-Y, Vignon-Clementel IE, and Marsden AL A comparison of outlet boundary treatments for prevention of backflow divergence with relevance to blood flow simulations. Computational Mechanics, 48:277–291, 2011.

[59]. Hughes TJR and Wells GN Conservation properties for the Galerkin and stabilised forms of the advection–diffusion and incompressible Navier–Stokes equations. Computer Methods in Applied Mechanics and Engineering, 194(9–11):1141–1159, 2005.

[60]. Bazilevs Y, Hsu M-C, Zhang Y, Wang W, Kvamsdal T, Hentschel S, and Isaksen J Computational fluid–structure interaction: Methods and application to cerebral aneurysms. Biomechanics and Modeling in Mechanobiology, 9:481–498, 2010. [PubMed: 20111978]

[61]. Hsu M-C and Bazilevs Y Blood vessel tissue prestress modeling for vascular fluid– structure interaction simulations. Finite Elements in Analysis and Design, 47:593–599, 2011.

[62]. Simo JC and Hughes TJR Computational Inelasticity Springer-Verlag, New York, 1998.

[63]. Kiendl J, Hsu M-C, Wu MCH, and Reali A Isogeometric Kirchhoff–Love shell formulations for general hyperelastic materials. Computer Methods in Applied Mechanics and Engineering, 291:280–303, 2015.

[64]. Lee C-H, Amini R, Gorman RC, Gorman III JH, and Sacks MS An inverse modeling approach for stress estimation in mitral valve anterior leaflet valvuloplasty for in-vivo valvular biomaterial assessment. Journal of Biomechanics, 47:2055–2063, 2014. [PubMed: 24275434]

[65]. Greco L and Cuomo M B-Spline interpolation of Kirchhoff–Love space rods. Computer Methods in Applied Mechanics and Engineering, 256:251–269, 2013.

[66]. Kamensky D, Xu F, Lee C-H, Yan J, Bazilevs Y, and Hsu M-C A contact formulation based on a volumetric potential: Application to isogeometric simulations of atrioventricular valves. Computer Methods in Applied Mechanics and Engineering, 330:522–546, 2018. [PubMed: 29736092]

[67]. Peskin CS Flow patterns around heart valves: A numerical method. Journal of Computational Physics, 10(2):252–271, 1972.

[68]. Peskin CS The immersed boundary method. Acta Numerica, 11:479–517, 2002.

[69]. Mittal R and Iaccarino G Immersed boundary methods. Annual Review of Fluid Mechanics, 37:239–261, 2005.

[70]. Sotiropoulos F and Yang X Immersed boundary methods for simulating fluid–structure interaction. Progress in Aerospace Sciences, 65:1–21, 2014.

[71]. Hughes TJR, Cottrell JA, and Bazilevs Y Isogeometric analysis: CAD, finite elements, NURBS, exact geometry, and mesh refinement. Computer Methods in Applied Mechanics and Engineering, 194:4135–4195, 2005.

[72]. Cottrell JA, Hughes TJR, and Bazilevs Y Isogeometric Analysis: Toward Integration of CAD and FEA John Wiley & Sons, Chichester, 2009.

[73]. Hughes TJR, Feijoó GR, Mazzei L, and Quincy JB The variational multiscale method–A paradigm for computational mechanics. Computer Methods in Applied Mechanics and Engineering, 166:3–24, 1998.

[74]. Hughes TJR, Mazzei L, and Jansen KE Large eddy simulation and the variational multiscale method. Computing and Visualization in Science, 3:47–59, 2000.

[75]. Hughes TJR, Oberai AA, and Mazzei L Large eddy simulation of turbulent channel flows by the variational multiscale method. Physics of Fluids, 13:1784–1799, 2001.

[76]. Hughes TJR and Sangalli G Variational multiscale analysis: the fine-scale Green's function, projection, optimization, localization, and stabilized methods. SIAM Journal of Numerical Analysis, 45:539–557, 2007.

[77]. Bazilevs Y, Calo VM, Cottrel JA, Hughes TJR, Reali A, and Scovazzi G Variational multiscale residual-based turbulence modeling for large eddy simulation of incompressible flows. Computer Methods in Applied Mechanics and Engineering, 197:173–201, 2007.

[78]. Tezduyar T, Aliabadi S, Behr M, Johnson A, and Mittal S Parallel finite-element computation of 3D flows. Computer, 26(10):27–36, 1993.

[79]. Johnson AA and Tezduyar TE Mesh update strategeies in parallel finite element computations of flow problems with moving boundaries and interfaces. Computer Methods in Applied Mechanics and Engineering, 119:73–94, 1994.

[80]. Stein K, Tezduyar T, and Benney R Mesh moving techniques for fluid–structure interactions with large displacements. Journal of Applied Mechanics, 70:58–63, 2003.

[81]. Stein K, Tezduyar TE, and Benney R Automatic mesh update with the solid-extension mesh moving technique. Computer Methods in Applied Mechanics and Engineering, 193: 2019–2032, 2004.

[82]. Bazilevs Y, Calo VM, Hughes TJR, and Zhang Y Isogeometric fluid–structure interaction: theory, algorithms, and computations. Computational Mechanics, 43:3–37, 2008.

[83]. Bazilevs Y and Hughes TJR Weak imposition of Dirichlet boundary conditions in fluid mechanics. Computers & Fluids, 36:12–26, 2007.

[84]. Barbosa HJC and Hughes TJR The finite element method with Lagrange multipliers on the boundary: circumventing the Babuška–Brezzi condition. Computer Methods in Applied Mechanics and Engineering, 85(1):109–128, 1991.

[85]. Chung J and Hulbert GM A time integration algorithm for structural dynamics with improved numerical dissipation: The generalized-α method. Journal of Applied Mechanics, 60:371–75, 1993.

[86]. Jansen KE, Whiting CH, and Hulbert GM A generalized-α method for integrating the filtered Navier-Stokes equations with a stabilized finite element method. Computer Methods in Applied Mechanics and Engineering, 190:305–319, 2000.

[87]. Tezduyar TE, Sathe S, and Stein K Solution techniques for the fully-discretized equations in computation of fluid–structure interactions with the space–time formulations. Computer Methods in Applied Mechanics and Engineering, 195:5743–5753, 2006.

[88]. Bazilevs Y, Takizawa K, and Tezduyar TE Computational Fluid–Structure Interaction: Methods and Applications John Wiley & Sons, Chichester, 2013.

[89]. Kamensky D, Hsu M-C, Yu Y, Evans JA, Sacks MS, and Hughes TJR Immersogeometric cardiovascular fluid–structure interaction analysis with divergence-conforming B-splines. Computer Methods in Applied Mechanics and Engineering, 314:408–472, 2017. [PubMed: 28239201]

[90]. Hopf RM Modeling of Highly Deformable Structures and Materials for Biomedical Applications PhD thesis, ETH Zurich, 2016.

[91]. N Azadani A and Tseng EE Transcatheter heart valves for failing bioprostheses: state-of-the-art review of valve-in-valve implantation. Circulation: Cardiovascular Interventions, 4 (6):621–628, 2011. [PubMed: 22186106]

[92]. Nguyen T, Nguyen H, Nguyen M, Komatsu S, and Michiels R Heart valve prosthesis and methods of manufacture and use, 2011 US Patent 7,914,569 B2.

[93]. Morganti S, Valentini A, Favalli V, Serio A, Gambarin FI, Vella D, Mazzocchi L, Massetti M, Auricchio F, and Arbustini E Aortic root 3D parametric morphological model from 2D-echo images. Computers in Biology and Medicine, 43(12):2196–2204, 2013. [PubMed: 24290936]

[94]. Saura D, Dulgheru R, Caballero L, Bernard A, Kou S, Gonjilashvili N, Athanas-sopoulos GD, Barone D, Baroni M, Cardim N, et al. Two-dimensional transthoracic echocardiographic normal reference ranges for proximal aorta dimensions: results from the EACVI NORRE study. European Heart Journal-Cardiovascular Imaging, 18(2):167–179, 2016. [PubMed: 27044913]

[95]. Roman MJ, Devereux RB, Kramer-Fox R, and O'Loughlin J Two-dimensional echocardiographic aortic root dimensions in normal children and adults. American Journal of Cardiology, 64(8):507–512, 1989. [PubMed: 2773795]

[96]. Bathe K-J and Bolourchi S Large displacement analysis of three-dimensional beam structures. International Journal for Numerical Methods in Engineering, 14(7):961–986, 1979.

[97]. Lo SH Geometrically nonlinear formulation of 3D finite strain beam element with large rotations. Computers & Structures, 44(1–2):147–157, 1992.

[98]. Romero I A comparison of finite elements for nonlinear beams: the absolute nodal coordinate and geometrically exact formulations. Multibody System Dynamics, 20(1):51–68, 2008.

[99]. Dvorkin EN, Onte E, and Oliver J On a non-linear formulation for curved timoshenko beam elements considering large displacement/rotation increments. International Journal for Numerical Methods in Engineering, 26(7):1597–1613, 1988.

[100]. Bruschi G, De Marco F, Martinelli L, and Klugmann S Corevalve® transcatheter self-expandable aortic bioprosthesis. Expert Review of Medical Devices, 10(1):15–26, 2013. [PubMed: 23278219]

[101]. Caballero A, Sulejmani F, Martin C, Pham T, and Sun W Evaluation of transcatheter heart valve biomaterials: biomechanical characterization of bovine and porcine pericardium. Journal of the Mechanical Behavior of Biomedical Materials, 75:486–494, 2017. [PubMed: 28826102]

[102]. Mega M, Marom G, Halevi R, Hamdan A, Bluestein D, and Haj-Ali R Imaging analysis of collagen fiber networks in cusps of porcine aortic valves: effect of their local distribution and alignment on valve functionality. Computer Methods in Biomechanics and Biomedical Engineering, 19:1002–1008, 2016. [PubMed: 26406926]

[103]. Yap CH, Saikrishnan N, Tamilselvan G, and Yoganathan AP Experimental technique of measuring dynamic fluid shear stress on the aortic surface of the aortic valve leaflet. Journal of Biomechanical Engineering, 133(6):061007, 2011. [PubMed: 21744927]

[104]. Mummert J, Sirois E, and Sun W Quantification of biomechanical interaction of transcatheter aortic valve stent deployed in porcine and ovine hearts. Annals of Biomedical Engineering, 41(3):577–586, 2013. [PubMed: 23161165]

[105]. Tezduyar TE, Takizawa K, Moorman C, Wright S, and Christopher J Space–time finite element computation of complex fluid–structure interactions. International Journal for Numerical Methods in Fluids, 64:1201–1218, 2010.

[106]. Takizawa K and Tezduyar TE Computational methods for parachute fluid–structure interactions. Archives of Computational Methods in Engineering, 19:125–169, 2012.

[107]. Wu MCH, Kamensky D, Wang C, Herrema AJ, Xu F, Pigazzini MS, Verma A, Marsden AL, Bazilevs Y, and Hsu M-C Optimizing fluid–structure interaction systems with immersogeometric analysis and surrogate modeling: Application to a hydraulic arresting gear. Computer Methods in Applied Mechanics and Engineering, 316:668–693, 2017.

- An immersogeometric analysis framework for transcatheter heart valves is proposed.

- Components of the transcatheter heart valves are parametrically modeled.

- Validation of the proposed structural and fluid mechanics methods is presented.

- The framework is applied to the simulation of transcatheter heart valves.

- Friction is considered to study the risk of migration.
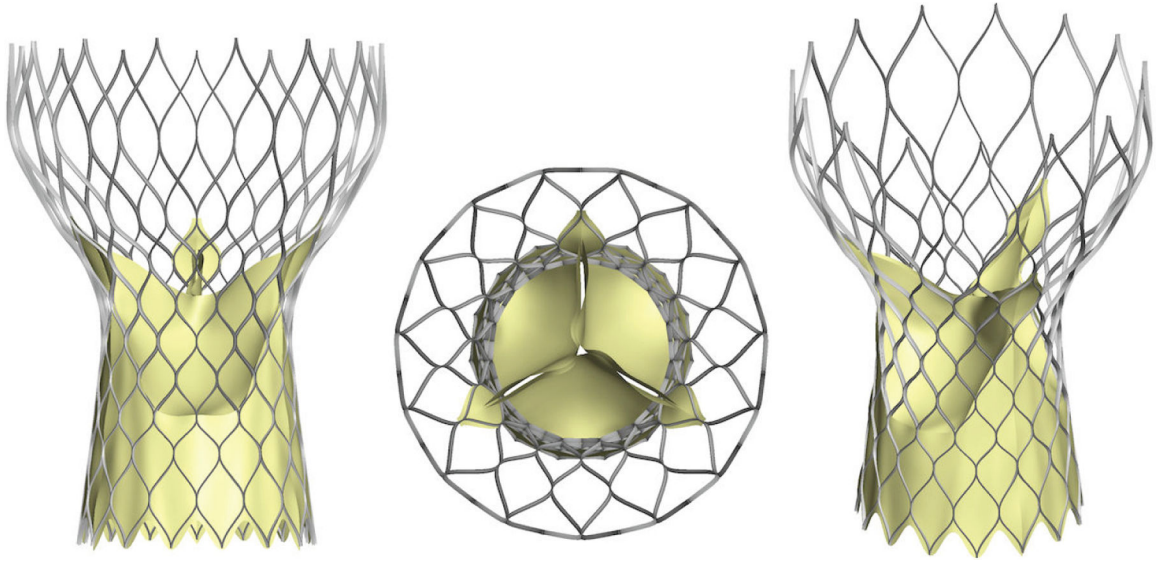
Figure 1:
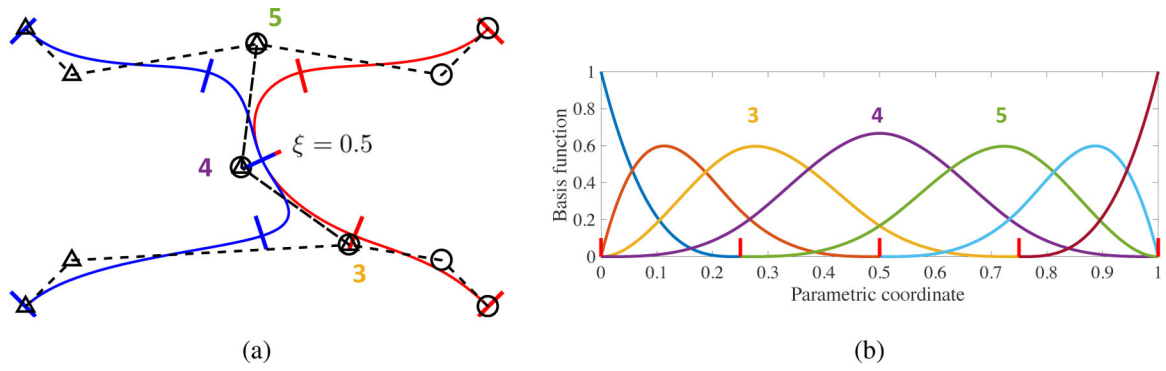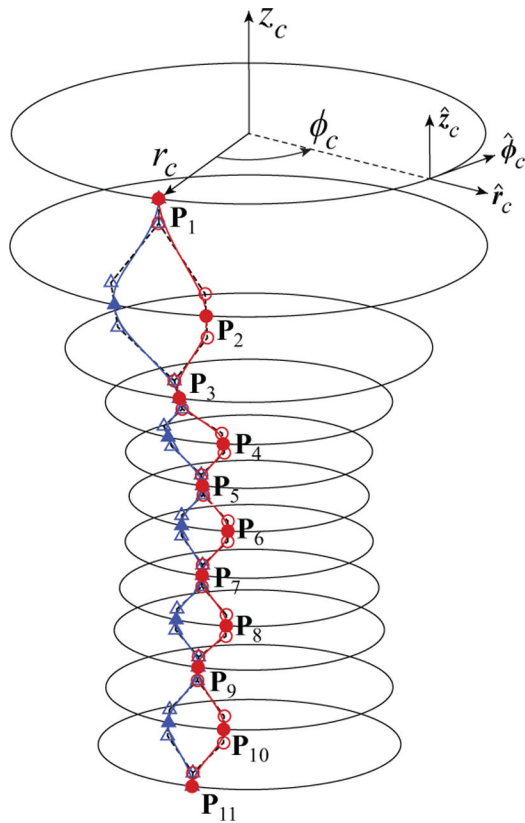Self-expandable CV26 modeled by cubic NURBS curves and surfaces.

Figure 2:
(a) Two cubic NURBS curves with three sets of overlapping control points to define one overlapping physical point. (b) Corresponding basis functions and knot vector.

	r_c (mm)	ϕ_c (°)	z_c (mm)
P_1	20.37	0	54.92
P_2	20.50	12	44.83
P_3	15.78	0	35.67
P_4	12.33	12	30.80
P_5	10.60	0	26.33
P_6	10.30	12	22.34
P_7	10.65	0	18.26
P_8	11.14	12	14.08
P_9	11.60	0	10.30
P_{10}	12.33	12	5.15
P_{11}	13.00	0	0.00

Figure 3:

Cylindrical coordinates definition of two NURBS curves that define two wires in the CV26 frame. Black dashed lines depict the control point polygon. Solid red markers represent the locations of P_1 to P_{11} that define the connection points on the CV26. Hollow markers represent the rest of control points that can be used to adjust the shape of the wire. The cylindrical coordinates of P_1 to P_{11} are listed in the table.
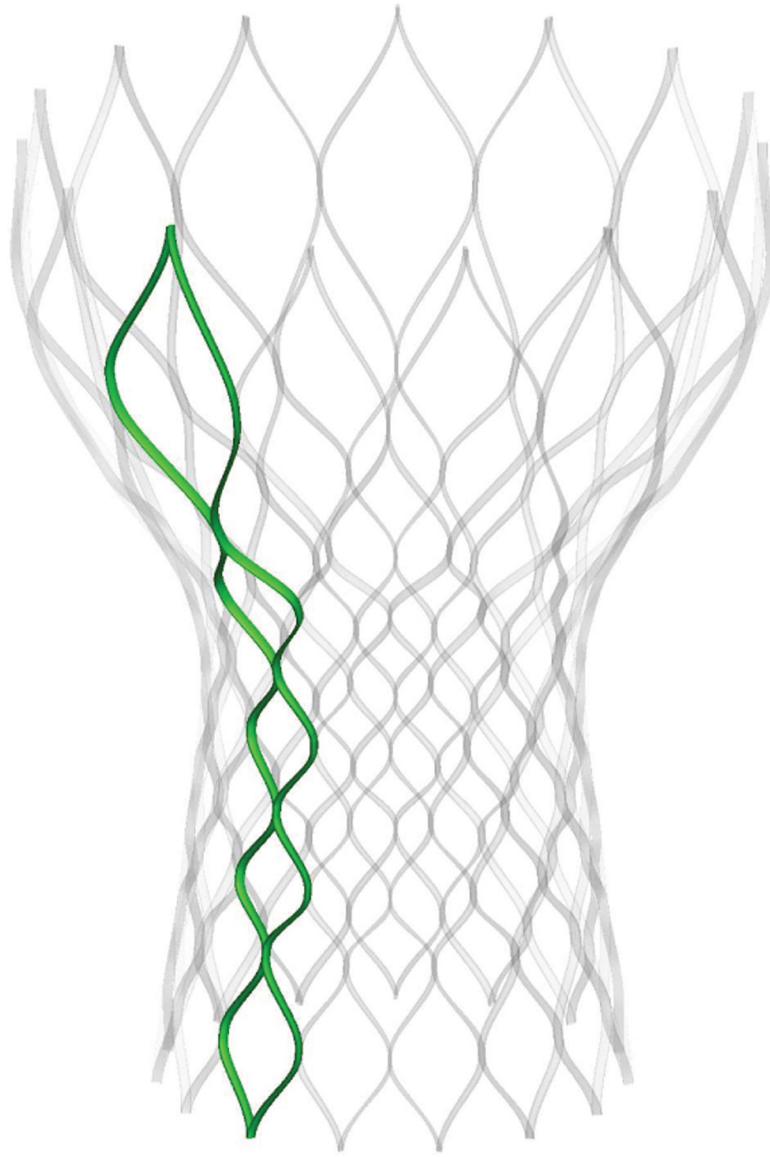
Figure 4:
Geometry of a perfectly radially symmetric CV26. The two initial wires, shown in green, are constructed first and radially repeated to construct the full frame geometry.
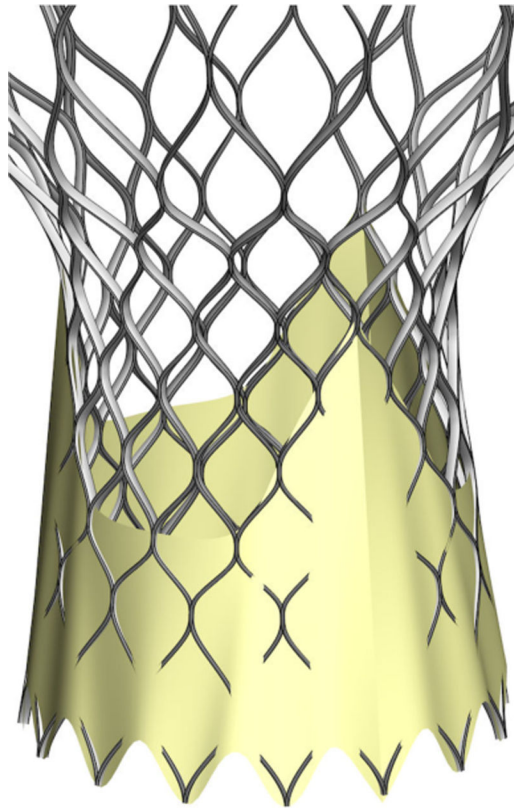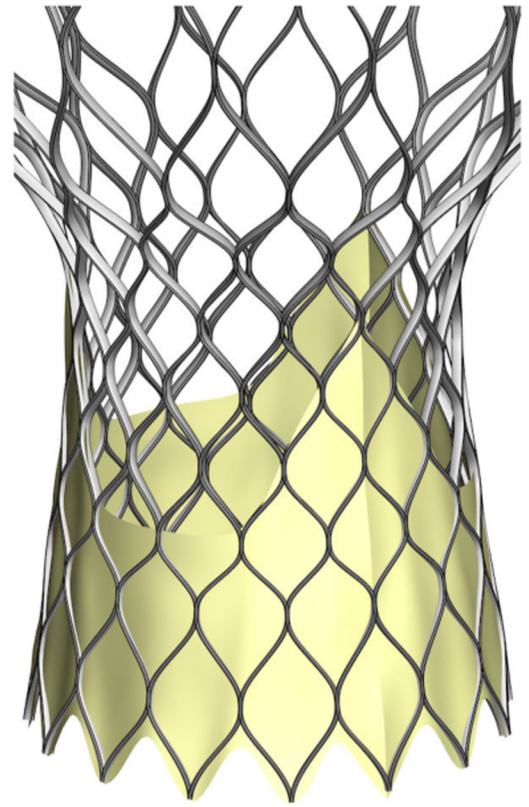
(a) Initial skirt design (b) Final skirt design

Figure 5:
Model of the skirt before and after the surfaces are penalized to match the frame geometry.

(a) Initial leaflet design (b) Final leaflet design
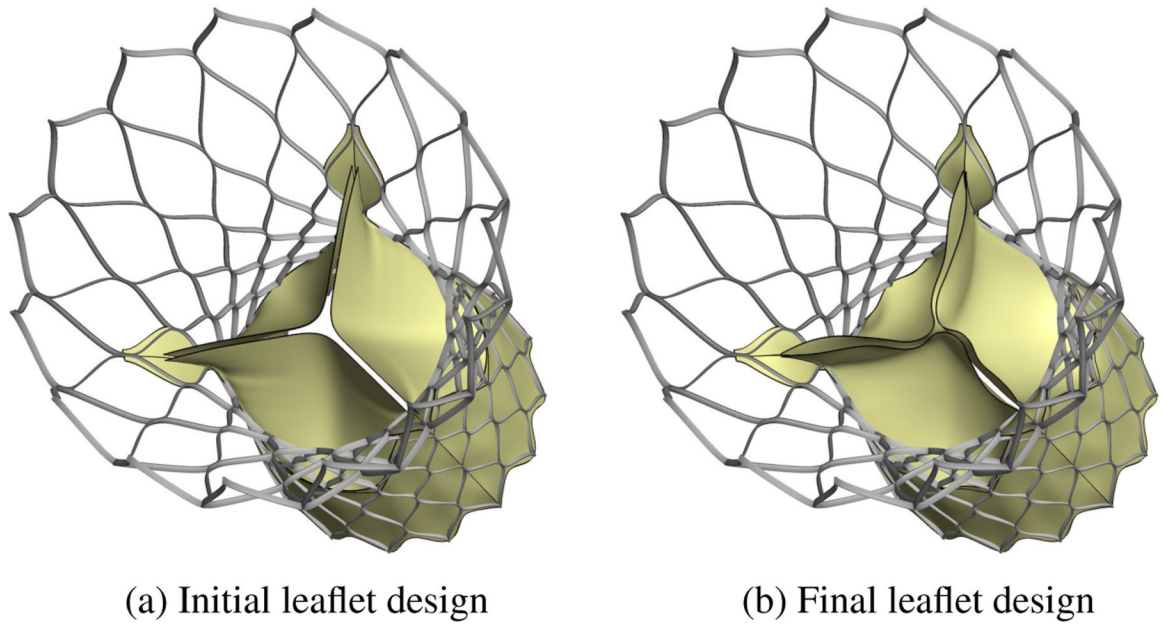
Figure 6:
Leaflet configuration before and after a pressure is applied to deform the geometry and obtain the new reference configuration used in the structural and FSI simulations.

(a) Skirt and commissural joints   (b) Leaflets and fiber orientation
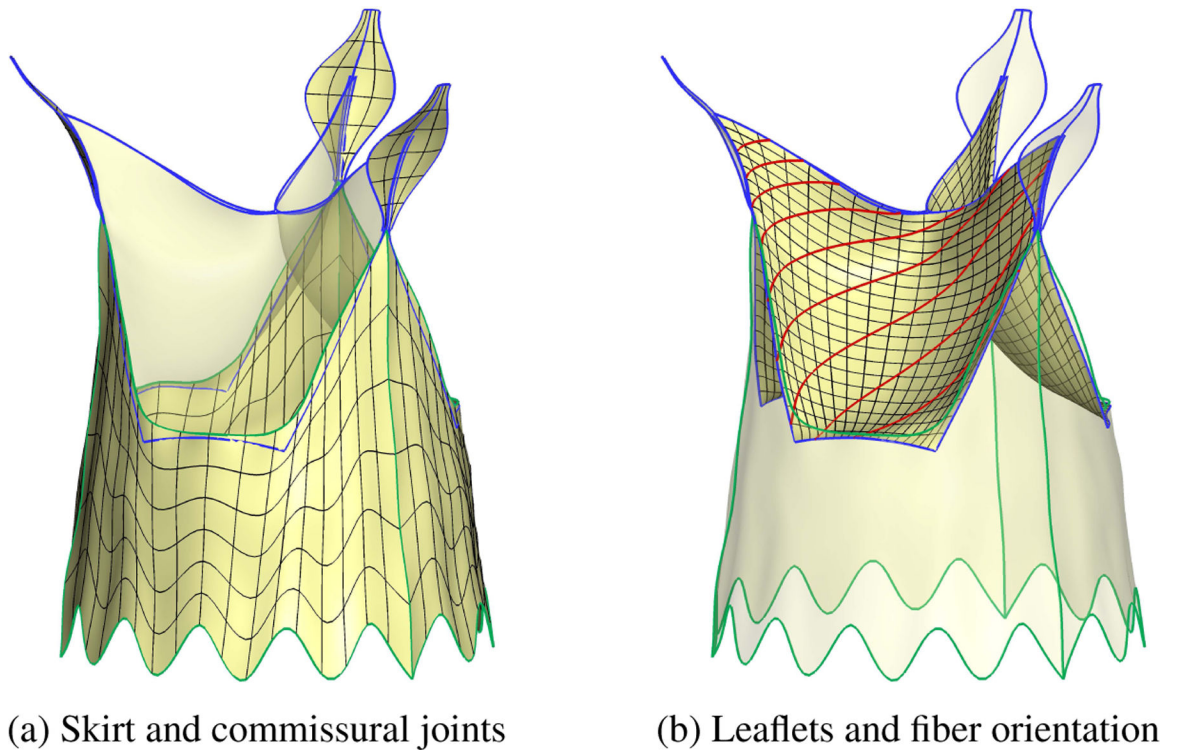
Figure 7:
Computational meshes of the final structures for the stress-free reference configuration.
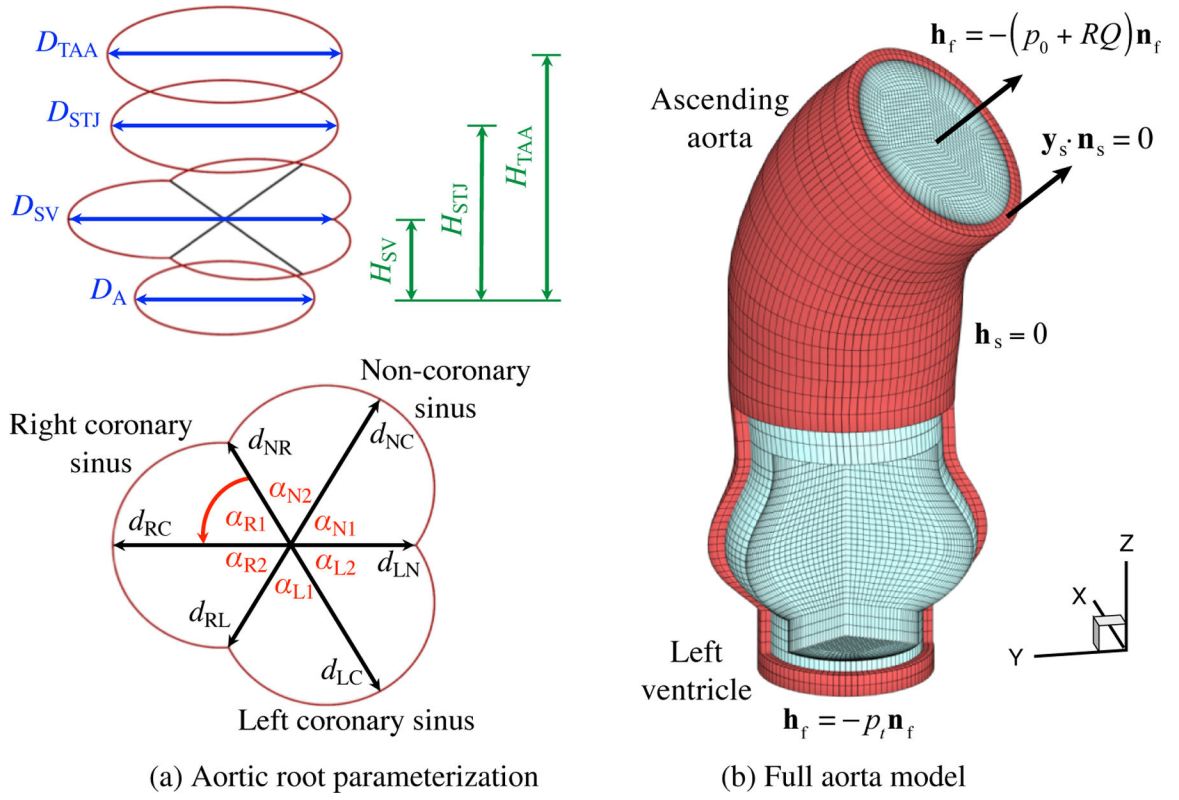
Figure 8:
Geometry modeling of the aorta, and the computational meshes and boundary conditions used in the FSI simulation.
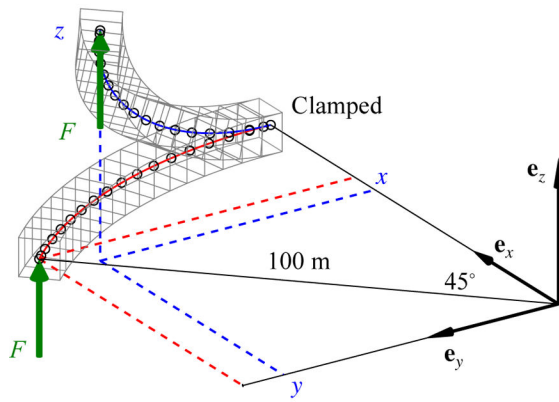
(a) Problem setup and simulation result
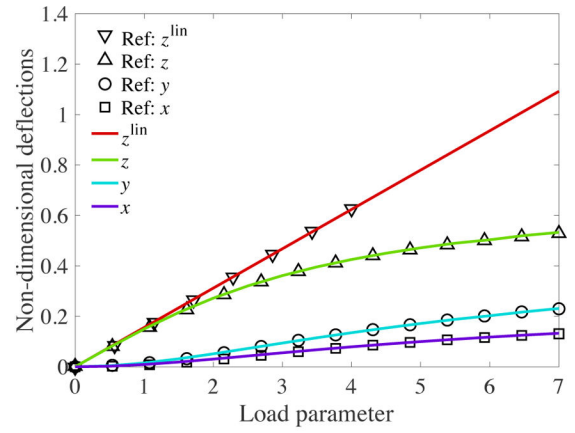
(b) Result comparison of the beam deflection

Figure 9:

The 45°-bending beam benchmark problem. The red curve in the problem setup shows the undeformed geometry, and the blue curve indicates the deformed geometry. The deformed configuration is shown at a load parameter of $k = 5$. The computed results for the beam deflection are compared to Bathe and Bolourchi [96].

(a) Connection point problem setup

(b) Side view of the beam configuration
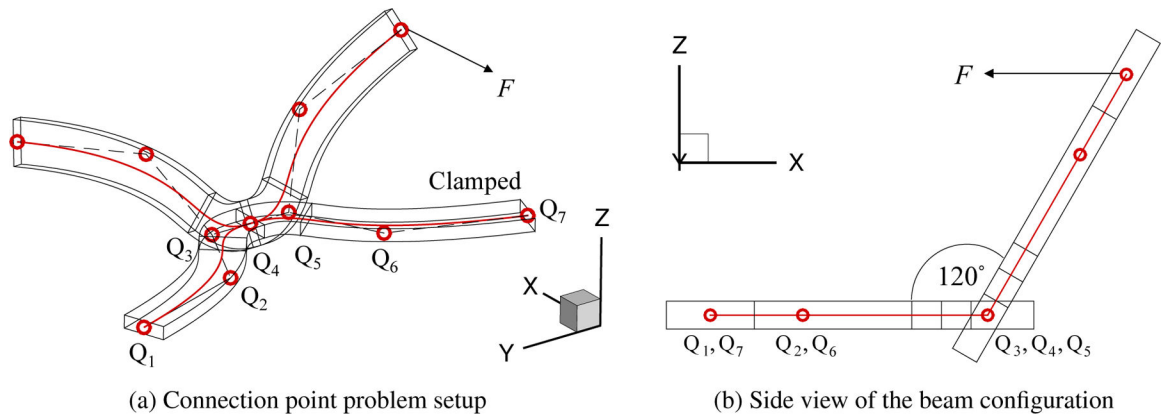
Figure 10:
Initial geometry and setup for the beam connection point problem, including the beam centerlines and control points.
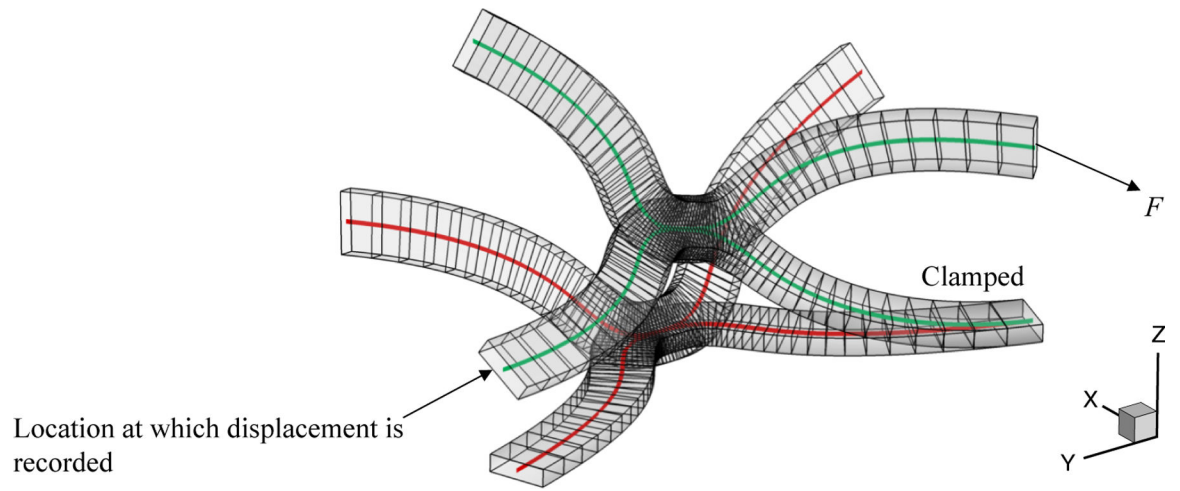
Figure 11:
Undeformed (red) and deformed (green) beam geometries for the connection point problem.

(a) Global *h*-refinement

(b) Local *h*-refinement
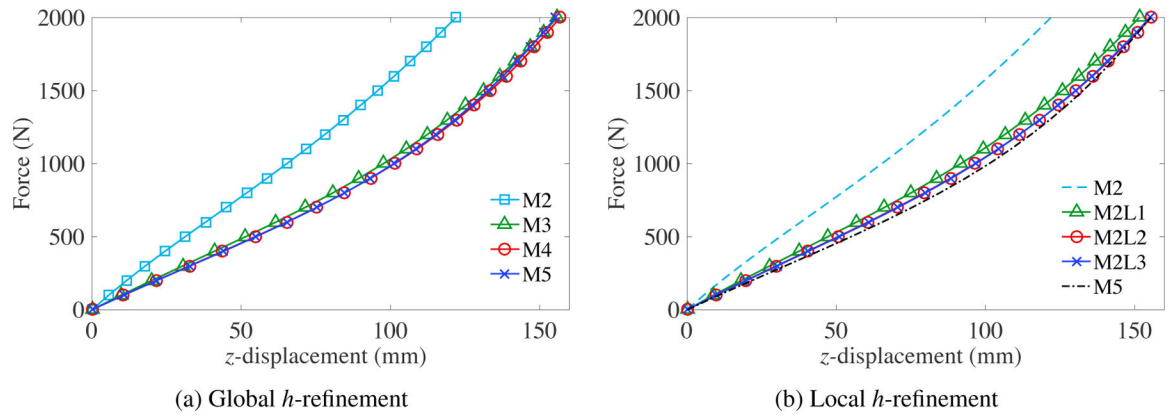
Figure 12:
Force versus *z*-displacement for the connection point problem using global and local *h*-refinement.

(a) M1

(b) M2

(c) M2L1

(d) M2L2
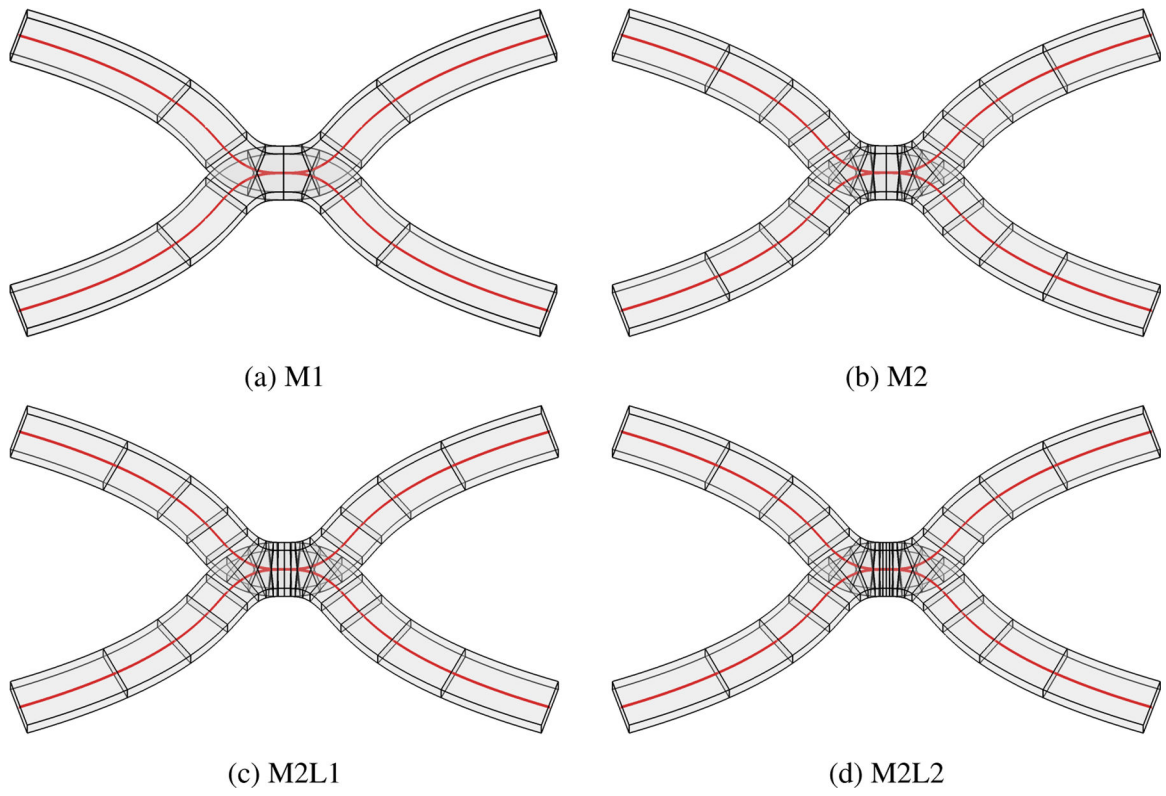
Figure 13:
Local *h*-refinement procedure used at the connection points.
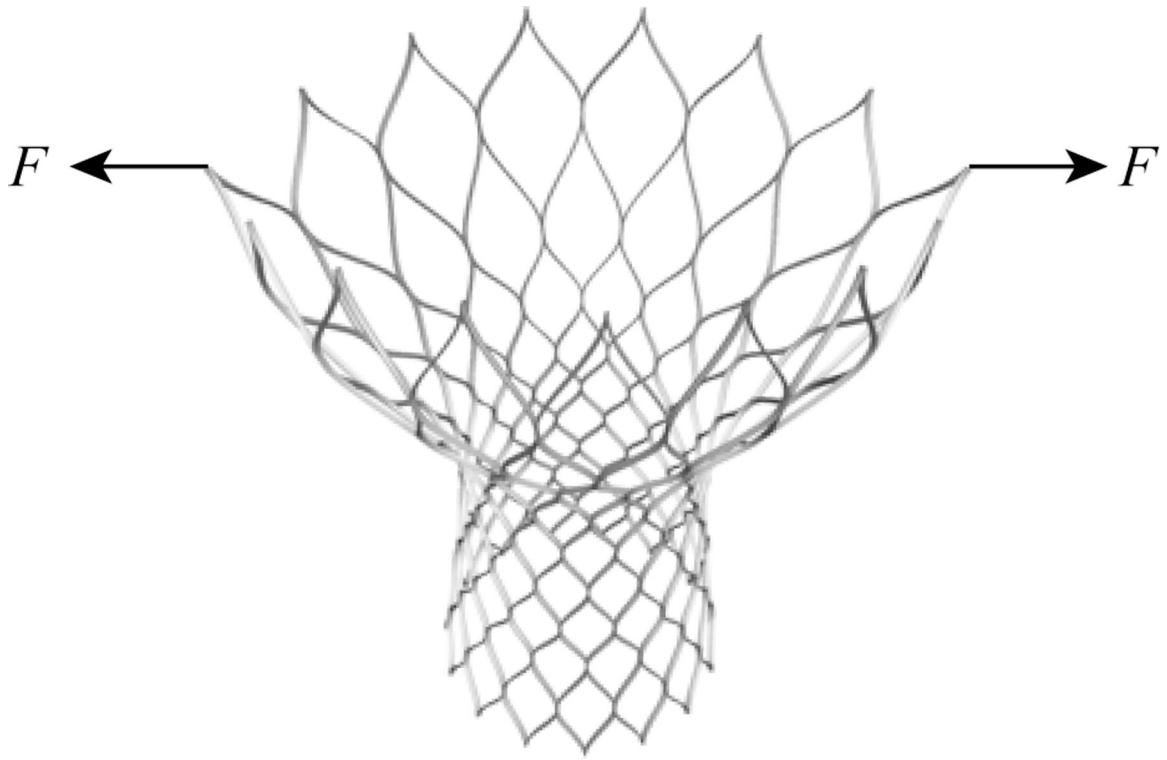
Figure 14:
Frame deformation under the tension forces.

(a) Global *h*-refinement

(b) Local *h*-refinement
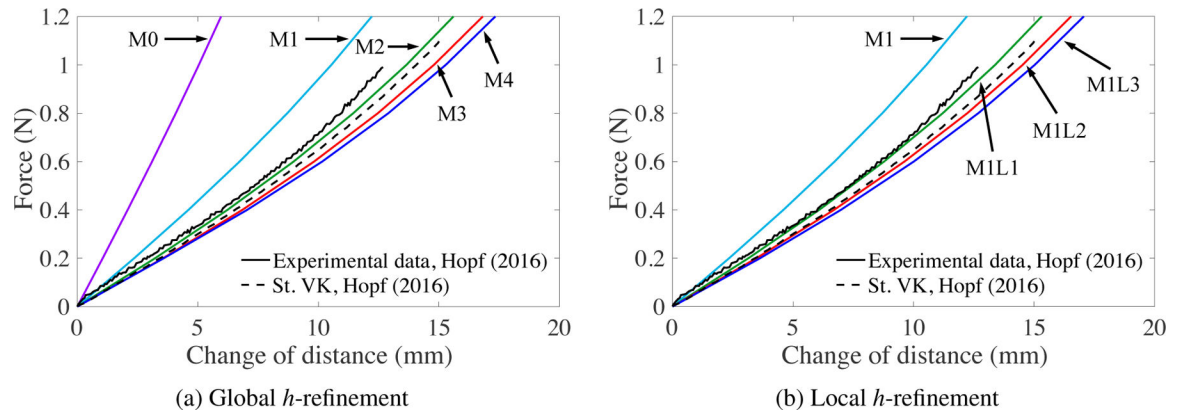
Figure 15:
Force versus the change of distance between the two points for the THV frame tension test using global and local *h*-refinement.

(a) Anisotropic case

(b) Isotropic case
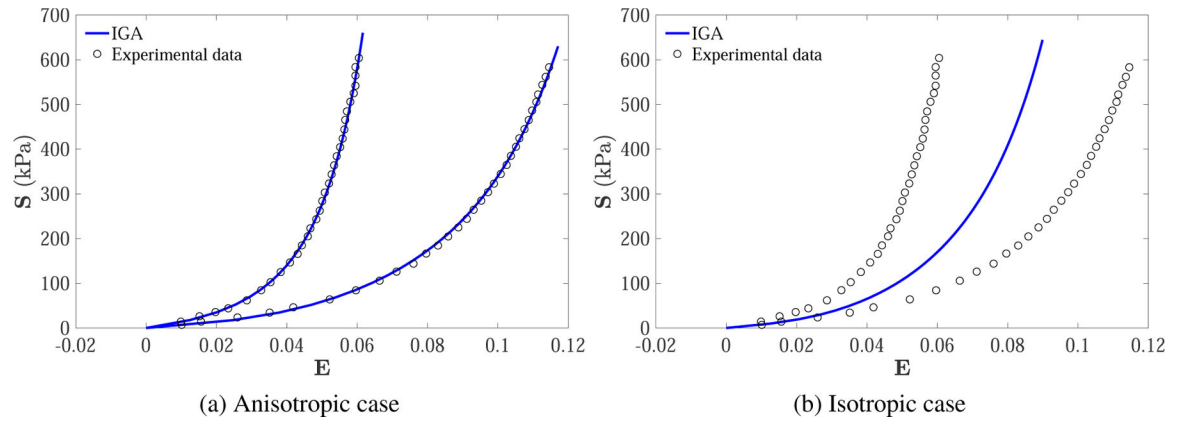
Figure 16:
Porcine pericardial material fitting results using the Lee–Sacks material model for experimental data reported in Caballero et al. [101].

(a) Crimped | (b) Deployed with FSI | (c) Deployed without FSI
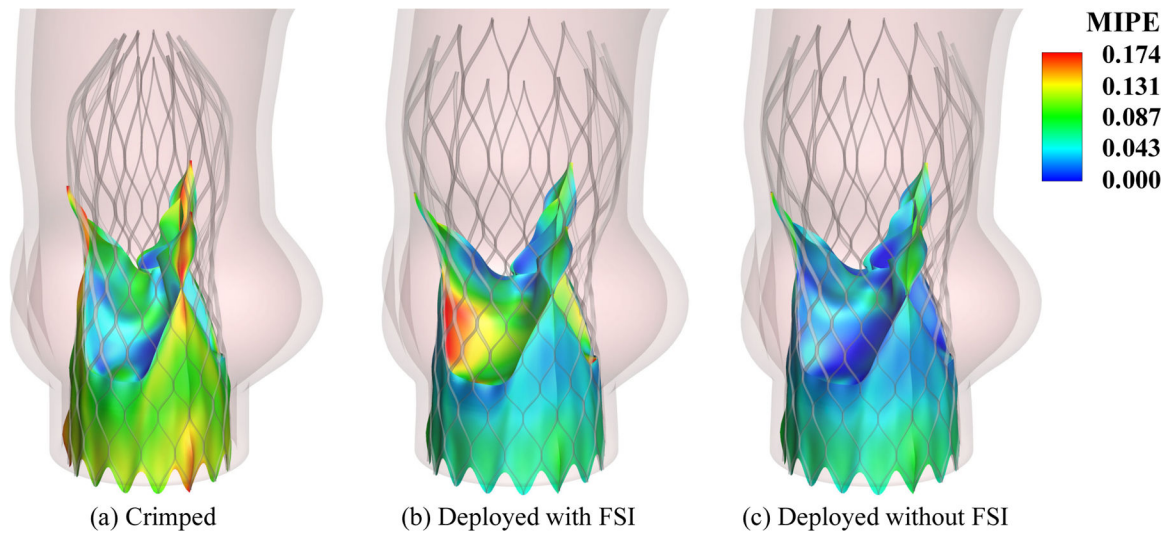
Figure 17:
The crimping process for deploying the CV26 at the annular location in the aorta. The leaflets and skirt are colored by the maximum in-plane principal Green–Lagrange strain (MIPE) evaluated on the outer side of the shells. The maximum strains on the leaflets, from the left figure to the right, are 0.162, 0.201, and 0.068, respectively.
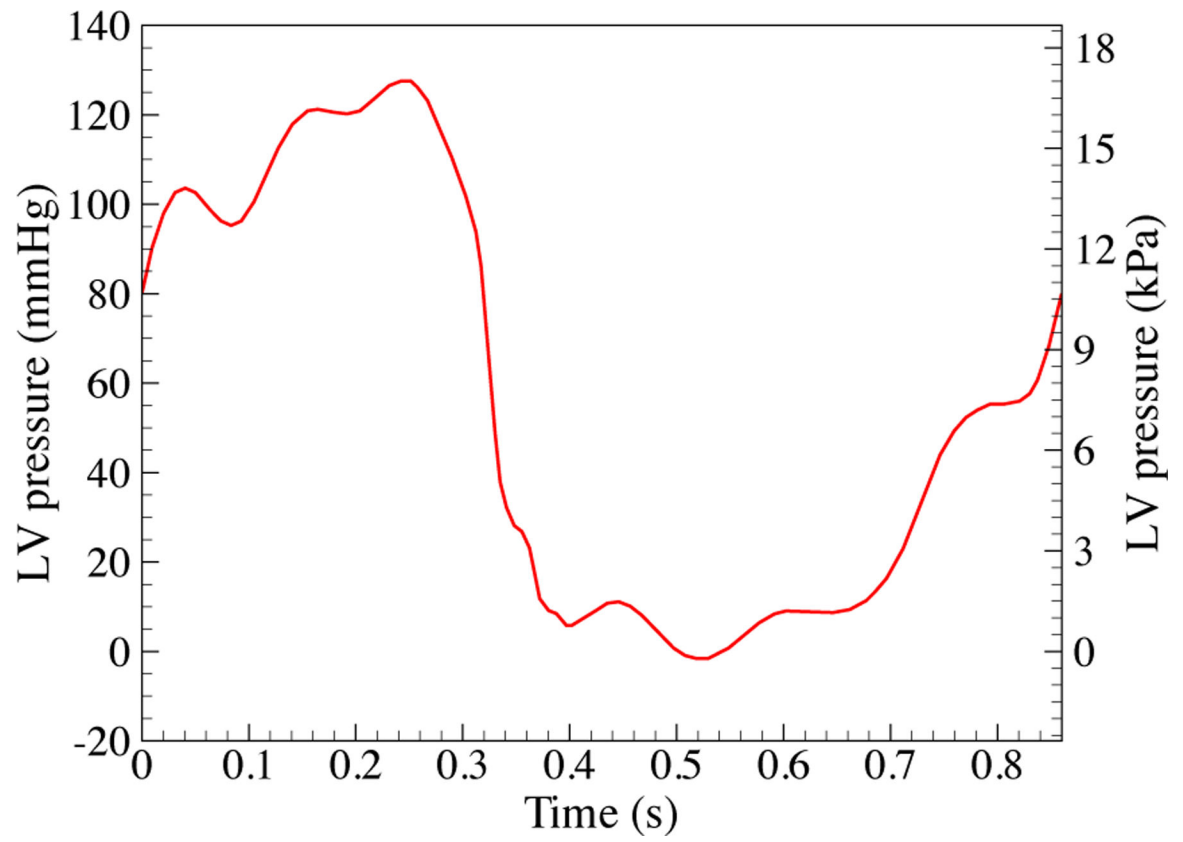
Figure 18:
The physiological left ventricular (LV) pressure profile, obtained from Yap et al. [103], is applied at the inlet of the fluid domain. The duration of a single cardiac cycle is 0.86 s.
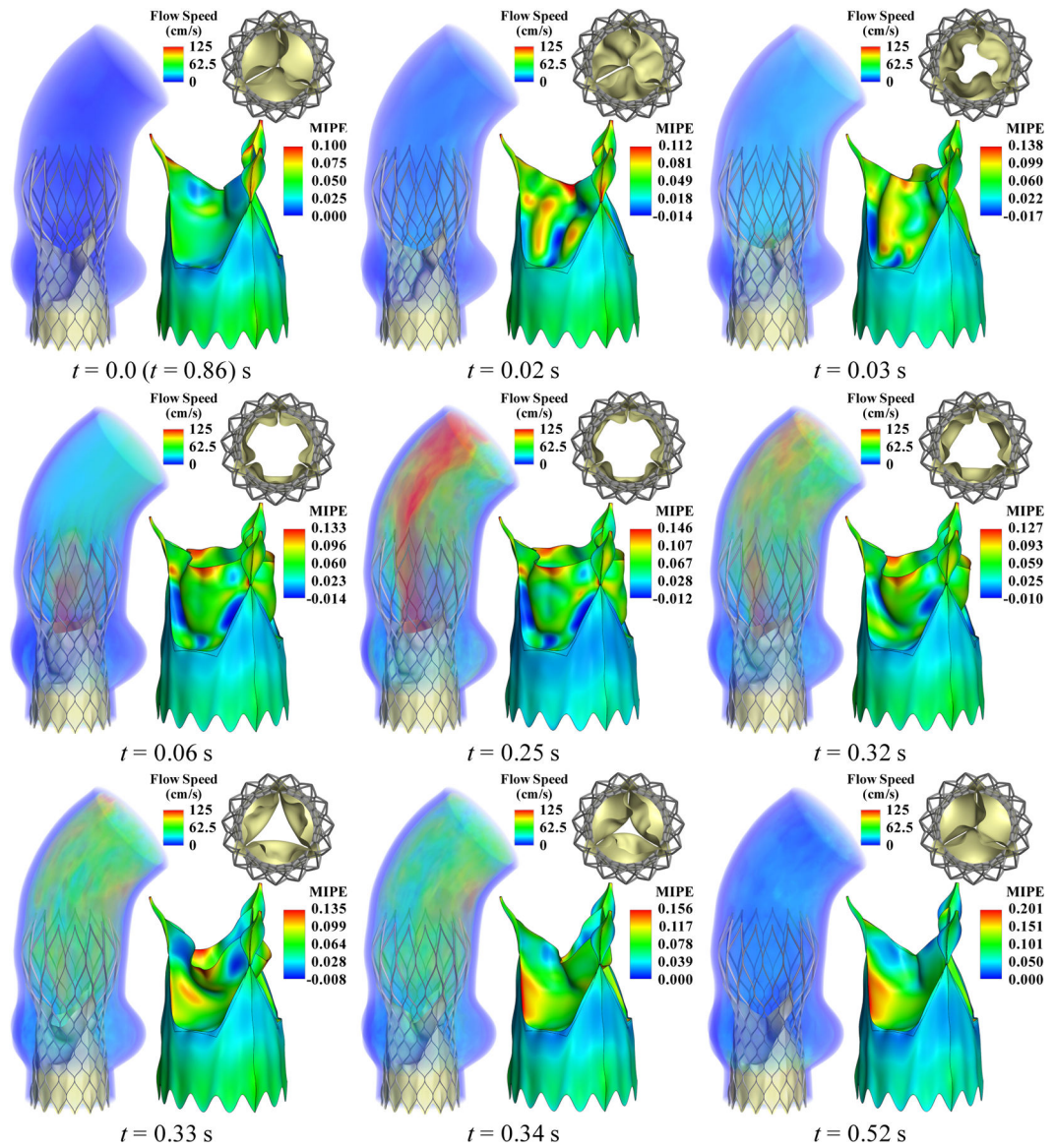
Figure 19:
Volume rendering of the velocity field at several points during a cardiac cycle. The time *t* is synchronized with Figure 18 for the current cycle. The strain map (MIPE) on the skirt and leaflets and the top view of the THV are also shown at each time. The strains are evaluated on the outer side of the shells.
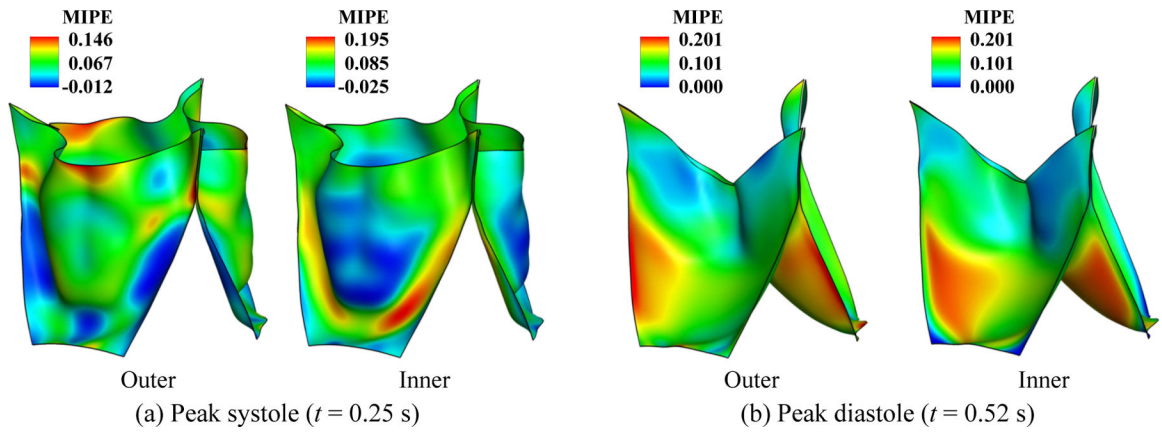
(a) Peak systole ($t = 0.25$ s) (b) Peak diastole ($t = 0.52$ s)

Figure 20:
MIPE evaluated on the outer and inner side of the leaflets at peak systole and peak diastole.
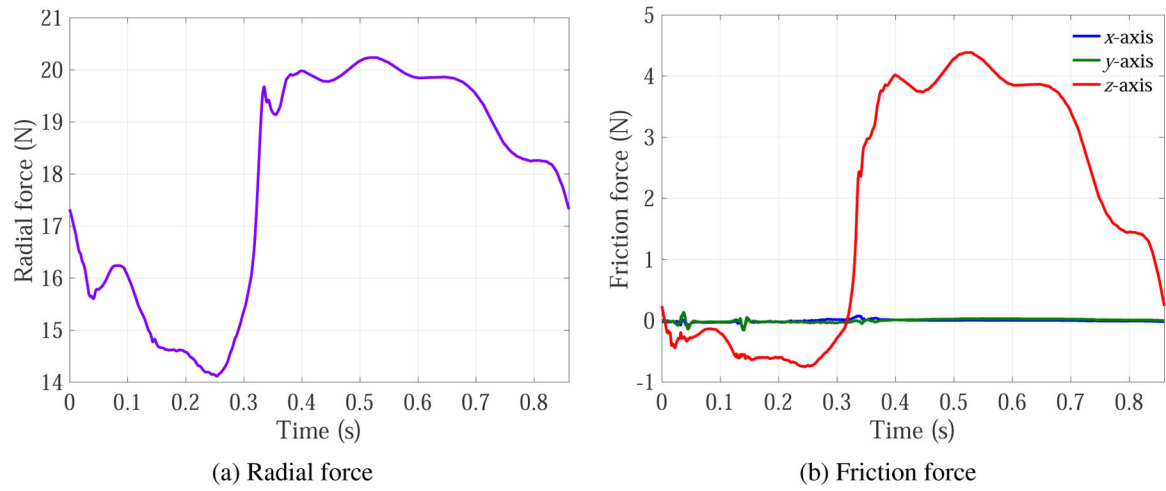
(a) Radial force

(b) Friction force

Figure 21:
The total radial and friction forces versus time from the FSI simulation of the CV26 over a cardiac cycle.
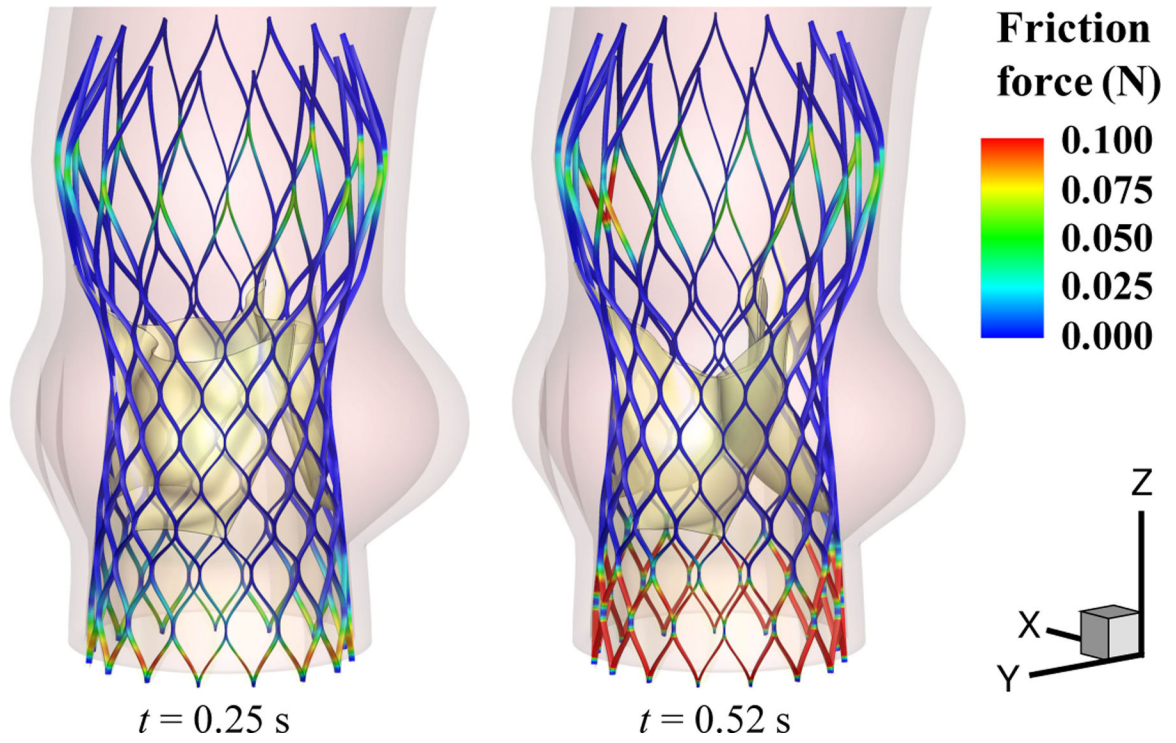
Figure 22:
The friction magnitude distribution at the fully-opened configuration ($t = 0.25$ s) and the fully-closed configuration ($t = 0.52$ s).
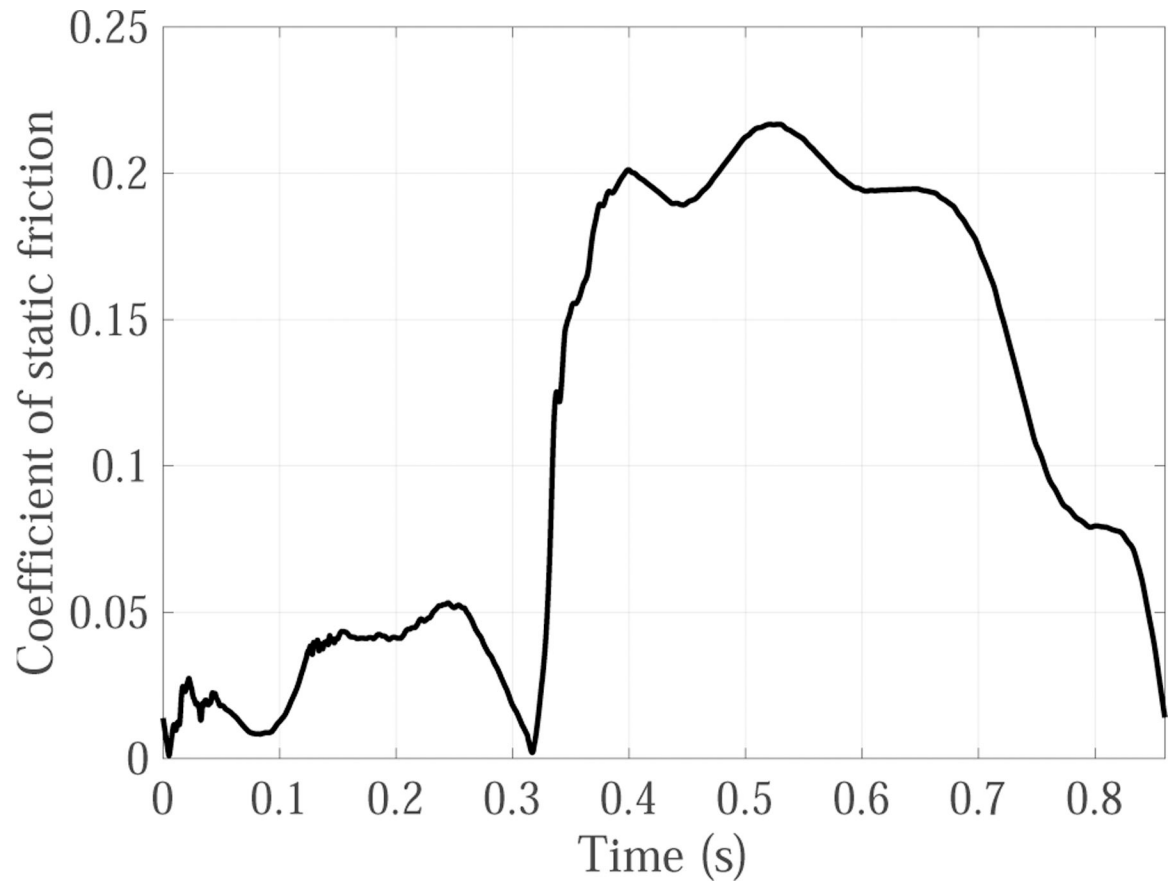
Figure 23:
Ratio of friction force magnitude to radial force magnitude over a cardiac cycle.

Table 1:

Aortic root dimensions

	All adults (12 patients) [93]	Male adults (68 patients) [94]	Male adults (310 patients) [95]	Selected parameters
D_A (mm)	20.5	26 ± 3	21.9 ± 2.2	23
D_{SV} (mm)	32.6	34 ± 3	33.6 ± 3.9	34
D_{STJ} (mm)	29.8	29 ± 3	28.7 ± 3.2	29
D_{TAA} (mm)	31.4	30 ± 4	29.9 ± 3.8	30
d_{RC}, d_{LC}, d_{NC} (mm)	18.8	–	–	20
d_{RL}, d_{LN}, d_{NR} (mm)	13.8	–	–	14
H_{SV} (mm)	10.9	–	–	11
H_{STJ} (mm)	24.4	–	–	24
H_{TAA} (mm)	34.2	–	–	34

Table 2:

List of coordinates of Q_1 to Q_7 for the connection point problem.

	x (mm)	y (mm)	z (mm)
Q_1	−300	500	0
Q_2	−200	200	0
Q_3	0	100	0
Q_4	0	0	0
Q_5	0	−100	0
Q_6	200	−200	0
Q_7	300	−500	0

Table 3:

Number of elements for each mesh in the connection point problem.

Global *h*-refinement		Local *h*-refinement	
M0	4		
M1	8		
M2	16		
M3	32	M2L1	18
M4	64	M2L2	20
M5	128	M2L3	22

Table 4:

Number of elements for each mesh in the frame tension test.

	Global *h*-refinement	Local *h*-refinement	
M0	840		
M1	1680		
M2	3360	M1L1	2280
M3	6720	M1L2	3480
M4	13340	M1L3	4080

Table 5:

Parameters for the contact problem.

	k_c **(dyn/cm)**	r_{max} **(cm)**
solid–beam	1.5×10^{10}	0.05
shell–beam	1.0×10^9	0.05
shell–shell	1.2×10^{11}	0.03